Journal of Physical and Chemical Reference Data

RESEARCH ARTICLE | JUNE 05 2026

# Rovibrational Energies of Carbon Dioxide with Kilohertz Accuracy

Fang-Hui Cao ; Chang-Le Hu; Zi-Tan Zhang; Ya-Qi Cheng ; Yan Tan ; An-Wen Liu ; Shui-Ming Hu



*J. Phys. Chem. Ref. Data* 55, 023101 (2026)
https://doi.org/10.1063/5.0322874

Journal of Physical and Chemical Reference Data ARTICLE pubs.aip.org/aip/jpr

# Rovibrational Energies of Carbon Dioxide with Kilohertz Accuracy

Cite as: J. Phys. Chem. Ref. Data 55, 023101 (2026); doi: 10.1063/5.0322874
Submitted: 14 January 2026 • Accepted: 23 April 2026 •
Published Online: 5 June 2026



Fang-Hui Cao,[1] Chang-Le Hu,[2] Zi-Tan Zhang,[2] Ya-Qi Cheng,[3] Yan Tan,[2] An-Wen Liu,[1,3,a)] and Shui-Ming Hu[1,2]

## AFFILIATIONS

[1] Hefei National Laboratory, University of Science and Technology of China, Hefei 230088, China
[2] Hefei National Research Center for Physical Sciences at the Microscale, University of Science and Technology of China, Hefei 230026, China
[3] State Key Laboratory of Chemical Reaction Dynamics, Department of Chemical Physics, University of Science and Technology of China, Hefei 230026, China

[a)] **Author to whom correspondence should be addressed:** awliu@ustc.edu.cn

## ABSTRACT

High-precision ro-vibrational spectroscopy of carbon dioxide isotopologues is essential for atmospheric remote sensing, climate studies, and fundamental molecular physics. Accurate determination of $CO_2$ vibrational-rotational energy levels is crucial for improving the reliability of relevant spectroscopic databases. We report a cavity-enhanced double-resonance spectroscopy technique stabilized by an optical frequency comb for precision measurement of weak rovibrational transitions in $CO_2$ isotopologues. By pumping a strong transition while probing a weak counterpart, the method enables sub-Doppler detection of 18 weak transitions in the 41 101–00 001 band with uncertainties of 4–52 kHz. Using complementary rovibrational models, we derived 394 and 133 experimental energy levels for $^{12}C^{16}O_2$ and $^{13}C^{16}O_2$, respectively, up to 14 170 $cm^{-1}$. These results, all from sub-Doppler measurements, provide significantly more accurate benchmarks than current spectroscopic databases and will improve atmospheric remote-sensing retrievals for climate and planetary science. The approach is generally applicable to other polyatomic molecules and opens a route to systematic precision spectroscopy of weak and forbidden transitions.

*Published by AIP Publishing on behalf of the National Institute of Standards and Technology.* https://doi.org/10.1063/5.0322874

## CONTENTS



## List of Tables

## List of Figures



## 1. Introduction

Carbon dioxide ($CO_2$) is a fundamental component of many planetary atmospheres[1] and plays a critical role in radiative balance, including that of Earth.[2] The rapid increase in atmospheric $CO_2$ concentration due to human activity[3] has made high-accuracy spectroscopic knowledge[4,5] essential for understanding climate change, the greenhouse effect,[6] the evolution of planetary atmospheres,[7] and enabling the quantitative retrieval of carbon sources and sinks.[8,9]

High-resolution spectroscopic data are indispensable for remote sensing missions monitoring $CO_2$, such as NASA's OCO-2 and OCO-3[10] and the European Space Agency's (ESA's) upcoming CO2M constellation.[11] While absorption bands of the main isotopologue $^{12}C^{16}O_2$ (626) are largely saturated in Earth's atmosphere, minor and asymmetric isotopologues, such as $^{13}C^{16}O_2$ (636) and $^{16}O^{12}C^{18}O$ (628), provide optically thin absorption features that are highly sensitive to concentration changes. These species are therefore crucial for accurately retrieving $CO_2$ column abundances and evaluating radiative forcing.

Beyond Earth, $CO_2$ spectroscopy supports atmospheric studies of Mars[12] and Venus,[13] where $CO_2$ dominates, and enables the characterization of exoplanetary atmospheres through transit and high-resolution ground-based spectroscopy. Isotopic variability across astrophysical environments further underscores the need for precise line positions and comprehensive line lists, especially for high-temperature applications.

Accurate experimental ro-vibrational energy levels are foundational for improving spectroscopic databases such as HITRAN,[4] CDSD (Carbon Dioxide Spectroscopic Databank),[14] the NASA Ames Research Center,[15] and ExoMol.[16] Continuous refinement of these databases relies on both advancements in effective Hamiltonian models[14] and the acquisition of new, high-precision experimental data.[17] A parallel and complementary approach involves constructing spectroscopic networks[18] using direct experimental measurements, which enables a model-independent determination of energy levels. This method, exemplified by the MARVEL (Measured Active Rotational-Vibrational Energy Levels) technique,[19] has yielded energy-level databases with sub-MHz accuracy for several key molecules, including water isotopes[20–24] $H_2^{16}O$ and $H_2^{18}O$, nine stable carbon dioxide isotopologues,[25–30] methane,[31] and other interstellar molecules.[32] Reliability of the databases has been verified through high-precision sub-Doppler spectroscopy. For instance, Lamb-dip measurements of $H_2^{17}O$ and $H_2^{18}O$ in the near-infrared, calibrated with an optical frequency comb, validated the reliability of the MARVEL energy levels for water, with agreement within 80 kHz.[33]

Despite this progress, achieving energy-level accuracy for the most abundant $CO_2$ isotopologues, $^{12}C^{16}O_2$ and $^{13}C^{16}O_2$, at the sub-MHz level comparable to that of water isotopologues presents a distinct spectroscopic challenge. As linear molecules with $D_{\infty h}$ symmetry, like other linear molecules with $D_{\infty h}$ symmetry, pure rotational transitions are forbidden due to the lack of a permanent electric dipole moment. Consequently, energy levels in $\Sigma_g^+$ vibrational states can only be accessed indirectly through hot bands. While recent high-precision work on another $D_{\infty h}$ molecule, acetylene ($C_2H_2$), has achieved sub-10 kHz accuracy in the near-infrared region using comb-calibrated cavity ring-down spectroscopy (CRDS),[34,35] extending such precision to $CO_2$ remains particularly difficult due to the weaker line strengths of its hot bands compared to those of acetylene. Pioneering work using saturated absorption spectroscopy (SAS) has established dozens of kHz-level frequency standards in the 9–10 μm region, derived from transitions in hot bands such as 00 011–10 001(2)[36,37] and 00 021–10 011(2)[38] of $CO_2$. Recent advances in optical-cavity-based techniques now enable intra-cavity laser intensities on the order of kW/cm$^2$ with only milliwatt-level input power.[39–41] This progress has expanded the application of SAS to transitions involving highly excited vibrational states,[42–46] achieving kHz-level frequency accuracy in the near-infrared region and opening new pathways for precision spectroscopy of $CO_2$.

However, measuring transitions with extremely weak absorption, such as those with Einstein coefficients as low as ~$10^{-6}$ s$^{-1}$, remains a significant challenge. Conventional spectroscopic techniques often require high laser power to achieve kHz- or MHz-level frequency accuracy, which can introduce spectral distortion[47] and limit measurement fidelity.

Double-resonance (DR) spectroscopy offers a powerful alternative for precisely measuring weak and forbidden transitions. This technique operates on a pump-probe principle: molecules are first excited to an intermediate state by a pump laser, and a subsequent probe laser monitors the associated radiative transition. The resulting signal depends on both the efficiency of the pump process and the Einstein coefficient of the probe transition. Recent advances have demonstrated the effectiveness of this approach for studying forbidden molecular transitions. For instance, in the mid-infrared region, Foltynowicz *et al.*[48–50] employed a ladder-type DR scheme to study the $3\nu_3$ and $2\nu_3$ band of $CH_4$, pumping the lower energy level with a mid-infrared difference-frequency source and probing with a second mid-infrared laser. Our research group

previously introduced a frequency-comb-locked cavity-enhanced DR scheme in the near-infrared, encompassing V-type, Λ-type, and ladder-type configurations. Using this setup, we have achieved[51] kHz-level measurement accuracy for transitions of the 3–0 band of $^{12}C^{16}O$. We have also applied a ladder-type scheme to measure transitions of the 60 025–30 013 band in $^{12}C^{16}O_2$, demonstrating the capability to selectively probe highly excited molecular states with high precision.[52]

The V-type and Λ-type configurations are particularly promising for enhancing the measurement of weak transitions, as they allow efficient optical pumping and sensitive detection with low probe power. In this work (TW), we implement a DR spectroscopic approach based on an optical frequency comb stabilized cavity-enhanced system. By pumping a strong transition while probing a weak counterpart, we obtain high signal-to-noise ratio spectra for weak transitions with substantially reduced laser power requirements. Combined with three independent ro-vibrational energy-level calculation schemes, this method enables us to determine the energy values for a total of 527 levels across 19 vibrational states of $^{12}C^{16}O_2$ and $^{13}C^{16}O_2$ molecules.

## 2. Method of V(Λ)-Type DR Spectroscopy

The principle of V-type and Λ-type DR spectroscopy method is based on pump-probe measurements involving three molecular energy levels, as illustrated in Fig. 1(a). In V-type DR spectroscopy, the pump laser at frequency $\omega_1$ excites molecules from a common lower state 0 to an upper state 1, while the probe laser at frequency $\omega_2$ monitors the population transfer from the same lower state 0 to a different upper state 2, thereby detecting the depletion of the shared lower state population. A similar mechanism applies to Λ-type DR spectroscopy. Assuming that the probe laser does not significantly perturb the population of the common energy level, and that under equilibrium (with the pump off) the populations of other upper (or lower) states are negligible, the depth of DR signal ($d_D$) can be approximated as:

$$d_{\mathrm{D}} \approx \beta \frac{I_{\mathrm{pump}} A_1 A_2 g_2'}{\Gamma^2} \frac{1}{\omega_1^4 \omega_2^2} \exp\left(-\frac{\Delta E}{k_B T}\right), \tag{1}$$

$$d_{\mathrm{S}} \approx \beta \frac{I A_2^2 g_2'}{2\Gamma^2} \frac{1}{\omega_2^6}. \tag{2}$$

Here, $A_1$ and $A_2$ are the Einstein-$A$ coefficients for the pump and probe transitions at frequencies $\omega_1$ and $\omega_2$, respectively; $g_2'$ denotes the statistical weight of the upper state in the probe transition; Γ represents the full width at half maximum (FWHM) of the sub-Doppler peak/dip. $I_{\mathrm{pump}}$ and $I$ are the pump laser intensities in the DR and SAS spectroscopy, respectively. $\Delta E$ is the low energy difference between the pump and probe transitions; $k_B$ is the Boltzmann constant; $T$ is experimental temperature, and $\beta$ is a parameter that consolidates fundamental constants, certain molecular properties unrelated to the considered transitions, and some experimental parameters. For comparison, the depth of saturated absorption ($d_S$) for the weak transition at $\omega_2$ is also given in Eq. (2). Detailed derivations can be found in Subsections 1 and 2 of the Appendix. It is obvious that the adoption of the DR spectroscopy brings critical advancements of $10^2$–$10^3$ reduction in required laser intensity or

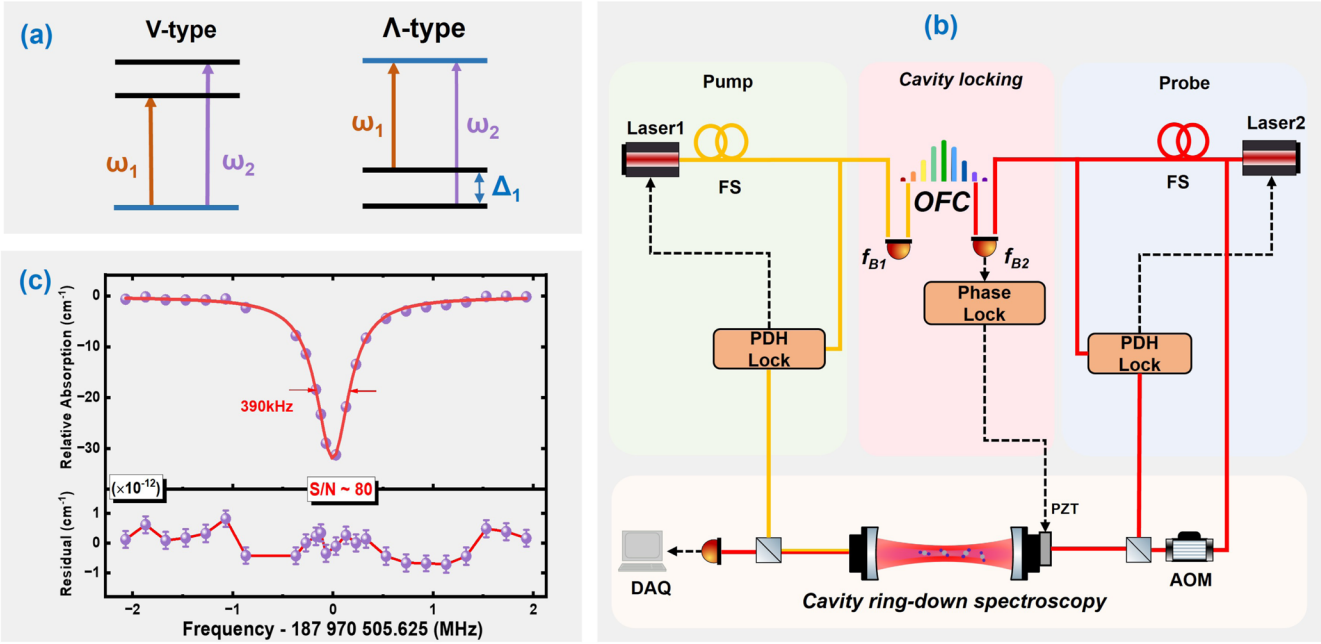


**FIG. 1.** (a) Energy level diagrams for V-type and Λ-type DR spectroscopy. (b) Schematic diagram of the cavity-locked optical frequency comb-assisted V-type DR spectroscopy experimental setup. FS: Fiber Splitter; AOM: Acousto-Optic Modulator; PDH: Pound–Drever–Hall; PZT: Piezoelectric Actuator; DAQ: Data Acquisition Card. (c)The COCA-DR V-type spectra of R(16) transition in the 41 101–00 001 band for $^{13}C^{16}O_2$ isotopologues, averaged from 480 scans at a pressure of ~0.8 Pa (signal-to-noise ratio ~ 80). Intra-cavity laser power: 23 W (pump) and 13 W (probe); Molecular speed along the laser propagating direction: 24.189(16) m/s.

the sub-Doppler depth enhancement by several order of magnitude compared to saturated spectroscopy for the transitions with extremely small Einstein-A coefficients ($A < 0.0001\ s^{-1}$).

## 3. Experiment

The comb-locked cavity-assisted DR (COCA-DR) absorption spectrometer is schematically depicted in Fig. 1(b), resembling configurations in prior studies.[51,52] The optical system utilizes two external-cavity diode lasers (Toptica DL100 Pro), locked to an optical cavity via the Pound–Drever–Hall (PDH) technique with modulation frequencies of 24.0 MHz (pump) and 22.6 MHz (probe). The cavity consists of high-reflectivity mirrors (radius of curvature ≈1 m) spaced 108 cm apart [free spectral range (FSR) ≈139 MHz], mounted within a temperature-stabilized Invar alloy spacer (<10 mK drift) in a vacuum chamber. The radius of pump and probe laser beam waists are approximate 0.5 mm, centered in the cavity.

For the DR measurements, the pump laser beam is split into two paths: one for PDH frequency locking and intra-cavity molecular excitation, and the other for beating with an optical frequency comb ($f_{B1}$) for precise frequency calibration. The probe laser is divided into three beams: the first for PDH locking, the second for comb beating ($f_{B2}$), and the third for CRDS probing. The CRDS probing beam, polarized perpendicularly to the locking beam, passes through an acousto-optic modulator (AOM) driven at a frequency exactly equal to the cavity FSR, enabling transmission during locking. The AOM provides a static extinction ratio of 50 dB, ensuring sufficient suppression of the main beam during ring-down events. A 300-Hz rectangular wave triggers the AOM to synchronize the ring-down events. The transmitted light is detected by a photodiode (PD), with polarizing optics – including Glan-Taylor prisms and polarizing beam splitters (extinction ratios of 40 and 30 dB, respectively) – separating the CRDS signal from the locking beam.[51] Experimental tests confirm that residual pump and probe locking beams contribute only a low and stable background, with negligible interference on the CRDS signal. The empty cavity exhibits a decay time $\tau_0 \approx 270$ μs (@1.59 μm), yielding mirror reflectivity $R \approx 0.999\,987$ and finesse $F \approx 241\,000$. The empty cavity transmittance was measured to be 8%, and the circulating laser power was estimated to be ~22 000 times the input.[39,53] Molecular absorption coefficients ($\alpha$) are derived according to the change in decay time via $\alpha = (c\tau)^{-1} - (c\tau_0)^{-1}$.

Laser frequencies are calibrated using an Er-fiber optical frequency comb. The comb's repetition frequency ($f_R \approx 200$ MHz) and carrier-envelope offset frequency ($f_0 \approx 250$ MHz) are locked to a local active hydrogen maser (VCH-1003M). A servo on a PZT-mounted high-reflective (HR) mirror locks $f_{B2}$ by adjusting the cavity length, thereby stabilizing both the cavity length and the two lasers to the comb. By changing the $f_{B2}$ setpoint in the PZT servo, we adjust the cavity length while simultaneously tuning both laser frequencies.

Here, a V-type DR occurs when two transitions have the same lower state, fulfilling the condition:[51,54]

$$\left(1 - \frac{\omega_{10}}{\omega_1}\right) + \left(1 - \frac{\omega_{20}}{\omega_2}\right) + \frac{v_p^2}{c^2} - \frac{\hbar(\omega_1 + \omega_2)}{2Mc^2} = 0, \tag{3}$$

where $\omega_1$ and $\omega_2$ are the frequencies of the pump and probe lasers, $\omega_{10}$ is the resonant frequency of the pump transition, $\omega_{20}$ is the resonant frequency of the probe transition, $v_p$ is the most probable speed, $c$ is the speed of light, $\hbar$ is the reduced Planck constant, and $M$ represents the molecular mass. If the frequency $\omega_{10}$ is known, we can use Eq. (3) to determine the probe transition frequency $\omega_{20}$. The velocity $v_z$ of molecules on resonance with the lasers, along the laser beam direction, can also be determined by this equation:[51]

$$\frac{v_z}{c} \approx 1 - \frac{\omega_{10}}{\omega_1} = \frac{\omega_{20}}{\omega_2} - 1, \tag{4}$$

where the high-order terms, such as the second-order Doppler shift and the recoil shift, were neglected.

A $^{13}C$ enriched carbon dioxide gas sample (from Wuhan Niuruid Gas Company), with a stated $^{13}CO_2$ abundance >99%, was subjected to "freeze-pump-thaw" purification prior to measurement. The COCA-DR spectra of 18 transitions in the 41 101–00 001 band of $^{13}CO_2$ were recorded at pressures in the range of 0.4–1.2 Pa.

Figure 1(c) displays the V-type COCA-DR spectra of the R(16) transition in the 41 101 band, centered near 6270.021 $cm^{-1}$. This transition was excited by a pump laser tuned close to the P(16) line in the 30 013–00 001 band, which shares the same lower energy level. Despite substantially lower circulating laser powers (pump: 23 W; probe: 13 W) compared to those used in previous SAS measurements (160 W),[47] the signal-to-noise ratio was improved by a factor of 14. The DR spectrum is well fitted by a symmetric Lorentzian profile, yielding a linewidth of ~390 kHz, less than half the value obtained via SAS.[47] The noise-equivalent absorption sensitivity (NEAS), defined as $\alpha_{min}\tau^{1/2}$ per spectral point in the DR spectrum, reaches $1.8 \times 10^{-11}$ $cm^{-1}$ $Hz^{-1/2}$. This result was obtained at 0.8 Pa with ~9 h of averaging (~480 scans), leading to a fitted residual root-mean-square (rms) of $5 \times 10^{-13}$ $cm^{-1}$ across a 4.4 MHz span comprising 24 points [see lower panel of Fig. 1(c)]. This corresponds to a 40-fold improvement over recent amplitude-modulated pump-based DR detection.[55]

## 4. Transition Frequencies From COCA-DR Spectroscopy

The uncertainty analysis for the absolute frequency of the R(16) transition is presented as follows, with contributions from individual sources summarized in Table 1.

**TABLE 1.** The uncertainty budget for the position of the R(16) line in the 41 101–00 001 band of $^{13}C^{16}O_2$ (unit: kHz)

| Source | Frequency | Uncertainty |
|---|---|---|
| Statistical | 187 970 490 461.5 | 2.4 |
| $\omega_{10}$ P(16) | | 1.0 |
| Frequency calibration | | 0.4 |
| Cavity locking servo | | 0.2 |
| Power shift | | <0.5 |
| Pressure shift | | 2.4 |
| Line profile asymmetry | | 0.8 |
| Second-order Doppler | 0.17 | ≪0.1 |
| Recoil shift | −3.4 | ≪0.1 |
| Total | 187 970 490 458.3 | 3.7 |

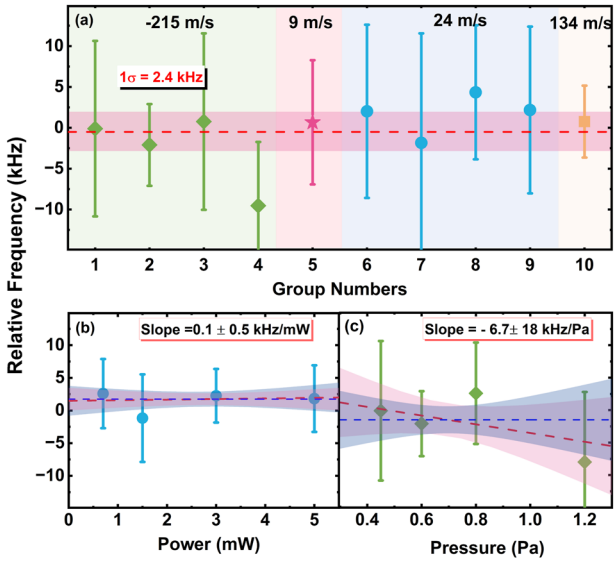


**FIG. 2.** (a) Transition frequency of the 41 101–00 001 band determined through multiple sets of DR spectroscopic measurements. (b) Center frequencies obtained from COCA-DR measurements under different injection laser powers but the same sample pressure of 0.8 Pa. (c) Center frequencies obtained from COCA-DR measurements under different sample pressures but the same injection laser power of 0.6 mW. Dashed lines denote the averaged values, while shaded regions represent standard deviations ($\pm 1\sigma$).

**Statistical:** Approximately 5400 V-type COCA-DR spectra of P(16)(30 013)/R(16)(41 101) were recorded across a pressure range of 0.4–1.2 Pa using input laser powers of 0.6–5 mW over ten independent runs. The total acquisition time was 100 h. The transition centers determined from different experimental conditions, corresponding to different $v_z$ values, −215, 9, 24, and 134 m/s, are plotted in Fig. 2(a). The averaged unperturbed frequency for R(16) is 187 970 490 461.5 kHz with a statistical uncertainty of 2.4 kHz.

**Frequency Calibration:** Owing to the frequency comb's phase lock to the hydrogen maser, we achieve a relative frequency accuracy better than $1 \times 10^{-12}$, corresponding to 0.2 kHz at 1.6 μm. During the spectral measurements, both the signal generator and frequency counter were referenced to a global positioning system (GPS)-disciplined Rubidium clock, with frequency uncertainties below 50 Hz. Both pump and probe laser frequencies were determined by beating with the optical frequency comb. As both laser frequencies are tuned simultaneously when scanning the cavity length, the overall frequency calibration uncertainty was estimated to be 0.4 kHz.

**Cavity Locking Servo:** The frequency uncertainty attributable to the cavity locking servo bias is ~0.2 kHz, based on the Allan deviation of the beat frequency between the probe laser and the frequency comb.

**Power Shift:** Figure 2(b) displays the relative frequencies of $\omega_2$ (corresponding to a velocity of 24 m/s along the laser axis) measured at four distinct input probe laser powers. The corresponding intracavity probe laser powers were calculated as 13–100 W under input powers of 0.6–5 mW. The saturation parameter $S$ for the P(16) pump transition was estimated to be 0.4, based on an intra-cavity pump laser power of 23 W. No significant power shift is observed, resulting in a systematic uncertainty of 0.5 kHz. This uncertainty is derived from the maximum shift estimated at the highest input laser power (5 mW).

**Pressure Shift:** Sample pressures ranging from 0.4 to 1.2 Pa were employed to investigate the pressure shift. Figure 2(c) shows the center probe frequencies obtained from the COCA-DR spectra measured at a molecular velocity of −215 m/s along the laser axis. A linear fit to the pressure-frequency relationship yields a slope of −6.7 ± 18 kHz/Pa, where the uncertainty exceeds the absolute value of the slope, indicating no significant pressure shift within the experimental uncertainty. The statistical uncertainties of the extrapolated zero-pressure frequency and the averaged frequency are 12.8 and 3.7 kHz, respectively. Considering these values along with other relatively small systematic contributions, we assign a systematic uncertainty of 2.4 kHz associated with the pressure shift analysis.

**Line Profile Asymmetry:** An asymmetric line profile was observed in the saturated absorption spectrum of some weak transitions,[56–59] which results in a frequency discrepancy of several hundred kilohertz among results obtained by using different profile models. Various mechanisms[47,59] have been proposed to explain this asymmetry. Here, the Fano line profile was also employed to fit the experimental COCA-DR spectrum. We obtained a $q$ factor of 0.01 and a frequency center shift of 0.8 kHz, indicating a negligible asymmetry. Consequently, we assign an uncertainty of 0.8 kHz due to imperfect line profile modeling.

**Second-order Doppler Shift:** In the COCA-DR measurements, the counter-propagating beam geometry eliminates the first-order Doppler shift, leaving only residual second-order Doppler contributions. For the $^{13}C^{16}O_2$ molecule at 298 K, the root-mean-square velocity of 406 m/s yields a calculated second-order Doppler shift of 0.17 kHz, with an uncertainty below 10 Hz.

**Recoil Effect:** The absorption of the probe and pump photons leads to recoil effects in the V-type DR measurement. The calculated recoil shifts are −1.65 kHz for the pump and −1.74 kHz for the probe, respectively. Therefore, the combined recoil shift in the V-type DR is −3.4 kHz.

Hence, combined with 1.0 kHz frequency uncertainty of $\omega_0$ determined in our previous work,[46] the overall uncertainty was 3.7 kHz, and the frequency of the R(16) line was determined to be 187 970 490 458.3 kHz.

According to Eq. (2), the COCA-DR depth of the studied transitions in the 41 101 cold band was approximately proportional to the line intensities under similar intra-cavity pump laser power, resulting in statistical uncertainties that differed by an order of magnitude between the strongest and weakest transitions. Incorporating the uncertainty budget discussed earlier, total uncertainties for the 18 measured transitions span 4–52 kHz. Table 2 summarizes the frequencies and uncertainties, along with Einstein-$A$ coefficients from the HITRAN database,[4] and numbers of measured spectra for all transitions in the 41 101 cold band.

Ground state combination differences determined from five P($J$+2)/R($J$) transition pairs in TW agree well with values calculated from SAS results in the 3001(1,2,3) cold bands.[46] The deviations listed in the last column of Table 2 lie within 1$\sigma$ combined

**TABLE 2.** Frequencies of the transitions in the 41 101–00 001 band of $^{13}C^{16}O_2$ determined in TW

| 30 013–00 001 P($J''$) | | | 41 101–00 001 P($J''$) and R($J''$) | | | | | |
|---|---|---|---|---|---|---|---|---|
| Transitions | $A^a$ ($10^{-5}$ $s^{-1}$) | $\nu^b$ (kHz) | Transitions | $J''$ | $A^a$ ($10^{-5}$ $s^{-1}$) | N[c] | $\nu$ (kHz) | $\delta^d$ (kHz) |
| P(6) | 325 | 183 318 822 003.3(13) | R(6) | 7 | 0.46 | 842 | 187 742 913 682(46) | |
| P(10) | 314 | 183 220 474 377.1(07) | R(10) | 11 | 1.05 | 830 | 187 834 562 172(20) | |
| P(14) | 310 | 183 119 579 327.8(18) | R(14) | 15 | 1.85 | 1028 | 187 925 386 929(09) | |
| P(16) | 308 | 183 068 171 004.8(10) | R(16) | 17 | 2.31 | 5400 | 187 970 490 458(04) | }−15(17) |
| P(18) | 308 | 183 016 118 170.1(10) | P(18) | 17 | 2.23 | 1042 | 187 151 730 915(16) | |
| | | | R(18) | 19 | 2.80 | 520 | 188 015 388 622(06) | }−9(11) |
| P(20) | 308 | 182 963 417 199.1(07) | P(20) | 19 | 2.69 | 864 | 187 103 102 679(09) | |
| | | | R(20) | 21 | 3.31 | 474 | 188 060 082 261(13) | }−4(18) |
| P(22) | 308 | 182 910 063 984.6(11) | P(22) | 21 | 3.16 | 1077 | 187 054 284 874(12) | |
| | | | R(22) | 23 | 3.84 | 668 | 188 104 572 537(09) | }−3(13) |
| P(24) | 308 | 182 856 053 922.4(07) | P(24) | 23 | 3.66 | 1000 | 187 005 280 203(08) | |
| P(26) | 309 | 182 801 381 954.7(09) | R(26) | 27 | 4.94 | 922 | 188 192 950 036(05) | |
| P(34) | 313 | 182 575 958 433.5(06) | P(34) | 33 | 6.13 | | 186 757 581 997(21) | |
| | | | R(34) | 35 | 7.11 | 490 | 188 367 370 425(10) | |
| P(38) | 316 | 182 459 112 366.8(10) | R(38) | 39 | 8.13 | 400 | 188 453 479 658(24) | }2(28) |
| P(40) | 318 | 182 399 629 975.8(08) | P(40) | 39 | 7.47 | 755 | 186 607 005 401(13) | |
| P(44) | 321 | 182 278 506 105.7(07) | R(44) | 45 | 9.48 | 550 | 188 581 405 120(19) | |
| P(50) | 327 | 182 091 294 074.6(12) | R(50) | 51 | 10.6 | 538 | 188 708 053 229(52) | |

[a]Einstein-A coefficients from the HITRAN database.[4]
[b]Frequency values from SAS.[46]
[c]Number of averaged scans.
[d]Difference between the ground state combination differences (GSCD), $E''(J+2) - E''(J) = \nu_{R(J)} - \nu_{P(J+2)}$, obtained by COCA-DR in TW and that from SAS measurements of the 3001(1,2,3) cold bands.[46] Values in parentheses are 1$\sigma$ combined uncertainties.



uncertainties, demonstrating kHz-level frequency accuracy for molecular weak transitions achieved through this strong-pump weak-probe COCA-DR technique.

Figure 3 displays frequency differences between values from the HITRAN2020 database[4] (circles), Ames2021 calculation[15] (stars), the Doppler-limited experimental values,[60] and the sub-Doppler experimental values obtained in this study. The deviations of two databases exhibit pronounced dependence on $J$, which increases progressively from 1.2 MHz at $J' = 7$–30.0 MHz at $J' = 40$, then decreases to 25.1 MHz at $J' = 51$. Note that the frequencies remain unchanged in the newly released HITRAN2024 database[61] compared to those in HITRAN2020.

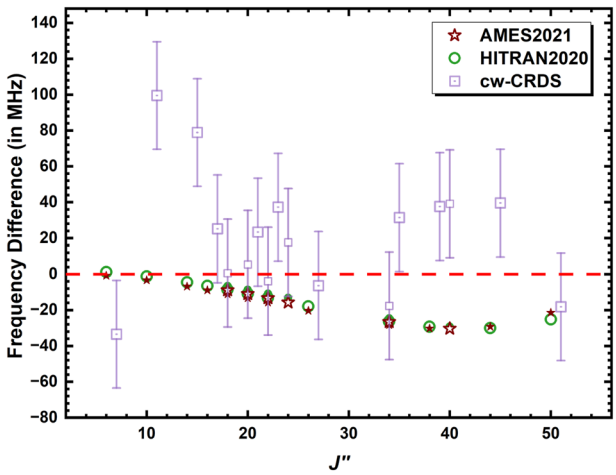


**FIG. 3.** The frequency differences between the sub-Doppler experimental values obtained in TW and those reported in HITRAN2020[4] (circles), Ames2021[15] (stars), and Doppler-limited experimental values[60] (squares) are plotted as a function of the lower rotational quantum number $J''$ for the transitions in the 41 101–00 001 band of $^{13}C^{16}O_2$.

## 5. Ro-Vibrational Energy Levels

The rotational energy levels $E(J'')$ of the ground state can be obtained from the ground-state combination differences $\Delta_2 F''(J) = \nu_{R(J-1)} - \nu_{P(J+1)}$, as shown for carbon dioxide with $D_{\infty h}$ symmetry in Fig. 4(a). For the $^{12}C^{16}O_2$ molecule, 36 experimental rotational levels were derived from 113 ground-state combination differences with experimental combined uncertainties better than 60 kHz. These combination differences were obtained from

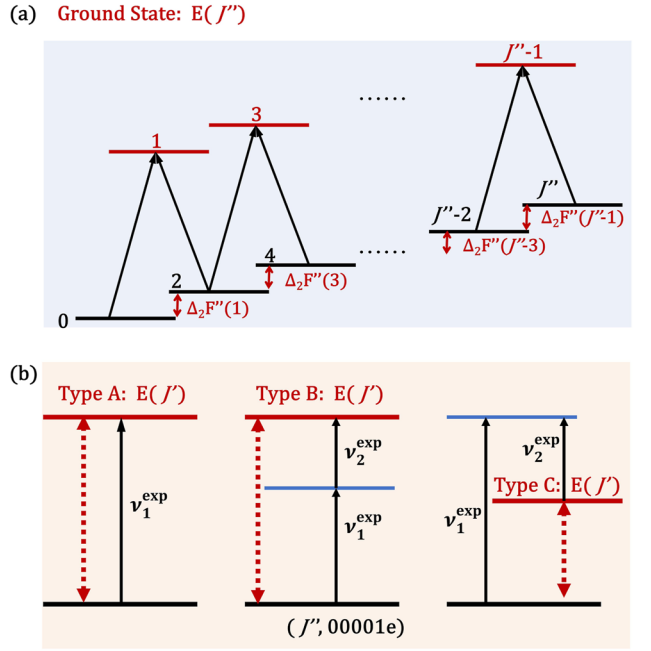


**FIG. 4.** Schematic for determining rotational energies. In panel (a), pure rotational energies E($J''$) are obtained by successively summing the ground-state combination differences $\Delta_2F''(J)$. In panel (b), rotational energies E($J'$) for the excited vibrational states are determined using three distinct approaches, designated as types A, B, and C.

saturation spectroscopy measurements of multiple vibrational cold bands, including 00 011,[62] 10 011(2),[63,64] 20 012(3),[44] and 30 012(3).[42,43,45] The ground-state energy levels were then determined by successively summing the $\Delta_2F''$ values according to

$$E(J'') = \Delta_2F''(1) + \Delta_2F''(3) + \cdots + \Delta_2F''(J''-1), \quad (5)$$

where the uncertainties were propagated using a weighted averaging approach. These levels, along with their associated uncertainties are listed in the second column of Table 3. For $^{13}C^{16}O_2$, however, the $\Delta_2F''$ values are discontinuous. Its rotational levels were therefore calculated using the ro-vibrational energy expression for an isolated vibrational state,

$$E(J) = G_v + B_vJ(J+1) - D_vJ^2(J+1)^2 + H_vJ^3(J+1)^3 + L_vJ^4(J+1)^4 + \cdots, \quad (6)$$

where $G_v$ represents the vibrational term, and $B_v$, $D_v$, $H_v$, $L_v$ are the rotational and centrifugal-distortion constants. The spectroscopic parameters were determined by fitting the experimental $\Delta_2F''$ values using Eq. (3) from Ref. 42 for the ground vibrational state.

For $^{12}C^{16}O_2$, the calculated ground-state rotational energy levels agree with the experimental values within the experimental uncertainties, with an uncertainty ratio of about 0.85 between calculated and experimental values. Therefore, the calculated pure rotational energy levels, together with their estimated uncertainties listed in Table 5, are used as an alternative input for retrieving the ro-vibrational energy levels of $^{13}C^{16}O_2$.

Figure 4(b) illustrates the procedure used to derive the experimental ro-vibrational energies for 17 excited vibrational states via three approaches:

**Type A:** $E(J') = E(J'') + \nu_1^{exp}$, corresponding to experimental frequencies for the following states: 00 011,[62] 10 011,[63] 10 012,[64] 20 012(3),[44] 30 012,[43,45] and 30 013[42] in $^{12}C^{16}O_2$; and 00 011,[65] 30 011(2,3),[46] 41 101 (TW) in $^{13}C^{16}O_2$.

**Type B:** $E(J') = E(J'') + \nu_1^{exp} + \nu_2^{exp}$, obtained by combining experimental frequencies with experimental ground-state rotational energy levels for 00 021[38,64] and 60 025[42,52] in $^{12}C^{16}O_2$, and for 00 041[65] in $^{13}C^{16}O_2$.

**Type C:** $E(J') = E(J'') + \nu_1^{exp} - \nu_2^{exp}$, derived by experimental frequency subtraction between two ro-vibrational transitions, then combing the experimental ground rotational energy levels for 10 001(2)[37,62] states in $^{12}C^{16}O_2$.

In total, 472 ro-vibrational energy levels with kHz accuracy are provided for $^{12}C^{16}O_2$ (Tables 3 and 4) and $^{13}C^{16}O_2$ (Table 5). The method used to retrieve the energy level is also specified in the footnotes of Tables 3–5 for each excited vibrational state.

For completeness, 55 ro-vibrational energy levels were calculated from the spectroscopic parameters obtained by fitting the experimental energy levels listed in Tables 3–5. Their uncertainties are not listed but are estimated to be lower than the maximum experimental uncertainty within the same vibrational state. It should be noted that for vibrational states known or suspected to be perturbed, the polynomial expansions were limited to fourth order or lower, and *rms* values consistent with the experimental uncertainties were adopted in modeling the experimental energy levels. Note that Fleurbaey *et al.*[44] observed a 15 kHz perturbation in the 20 012, $J$ = 43 level, attributed to a weak interaction with the 04 411, $J$ = 43 level of $^{12}C^{16}O_2$. The perturbed or potentially perturbed states include: for $^{12}C^{16}O_2$ – 30 012 ($J$ = 23–67) and 60 025 ($J$ = 2–20); and for $^{13}C^{16}O_2$ – 30 011 ($J$ = 1–29), 30 012 ($J$ = 1–25), and 41 101 ($J$ = 7–25). In all cases, the full range of $J$ values listed was included in the fit. The spectroscopic parameters for the 17 vibrational states are summarized in Table 6, along with the root-mean-square (rms) fit error, the highest measured rotational quantum number $J_{max}$, the number of experimentally determined energy levels or combination differences ($N$), and the number of data points included in the fit.

## 6. Comparison With Literature

The MARVEL group has validated experimental positions and constructed empirical energy levels for seven carbon dioxide isotopologues ($^{12}C^{16}O_2$,[25] $^{13}C^{16}O_2$,[26] $^{16}O^{12}C^{18}O$,[27] $^{16}O^{13}C^{18}O$,[28] $^{12}C^{18}O_2$, $^{17}O^{12}C^{18}O$ and $^{13}C^{18}O_2$,[29] $^{16}O^{13}C^{17}O$ and $^{12}C^{17}O_2$[30]) using published literature. The associated uncertainties were estimated to be consistent with the experimental uncertainties of the measured transitions. Recently, Kochanov and Perevalov have also updated the CDSD-2024-PI (CDSD)[17] for $^{12}C^{16}O_2$ with new experimental data obtained after the 2019 version of CDSD-296.[14] Notably, the line frequencies for $^{12}C^{16}O_2$ in the HITRAN2024 database have been updated using the CDSD-2024-PI dataset. We have compared the

**TABLE 3.** High-precision ro-vibrational energy levels of $^{12}C^{16}O_2$: (I) symmetric vibrational states (unit: $cm^{-1}$)

| $J$ | 00 001 | 00 021[a] | 10 001[a] | 10 002[a] | 60 025[a] |
|---|---|---|---|---|---|
| 0 | 0.0 | 4673.325 381 36 | 1388.184 196 49(72) | 1285.408 216 98(72) | 12 252.712 826 30 |
| 2 | 2.341 308 91(05) | 4675.629 773 41 | 1390.525 324 56(10) | 1287.751 103 80(10) | 12 255.030 399 31(14) |
| 4 | 7.804 325 73(06) | 4681.006 650 77 | 1395.987 927 80(10) | 1293.217 798 95(10) | 12 260.437 984 20(14) |
| 6 | 16.388 960 84(07) | 4689.455 925 52(41) | 1404.571 927 46(12) | 1301.808 195 33(12) | 12 268.935 376 07(14) |
| 8 | 28.095 073 39(08) | 4700.977 455 93(46) | 1416.277 202 14(12) | 1313.522 126 95(12) | 12 280.522 266 23(14) |
| 10 | 42.922 471 25(08) | 4715.571 051 73(47) | 1431.103 586 51(12) | 1328.359 367 72(12) | 12 295.198 257 53(14) |
| 12 | 60.870 911 23(09) | 4733.236 468 09(47) | 1449.050 870 88(12) | 1346.319 630 99(12) | 12 312.962 880 48(14) |
| 14 | 81.940 098 80(09) | 4753.973 418 10(63) | 1470.118 802 19(12) | 1367.402 570 56(12) | 12 333.815 615 66(15) |
| 16 | 106.129 688 31(10) | 4777.781 554 14(35) | 1494.307 081 51(12) | 1391.607 778 18(12) | 12 357.755 910 66(15) |
| 18 | 133.439 282 80(10) | 4804.660 480 36(50) | 1521.615 369 03(10) | 1418.934 788 54(10) | 12 384.783 197 21(16) |
| 20 | 163.868 434 29(11) | 4834.609 754 32(31) | 1552.043 279 11(12) | 1449.383 074 88(12) | 12 414.896 907 14(17) |
| 22 | 197.416 643 42(12) | 4867.628 876 69(47) | 1585.590 382 39(09) | 1482.952 048 84(10) | 12 448.096 485 41(17) |
| 24 | 234.083 359 76(12) | 4903.717 299 49(50) | 1622.256 206 73(12) | 1519.641 065 65(12) | 12 484.381 398 99(18) |
| 26 | 273.867 981 68(13) | 4942.874 425 09(30) | 1662.040 235 93(12) | 1559.449 418 83(12) | 12 523.751 145 63(18) |
| 28 | 316.769 856 33(13) | 4985.099 604 94(35) | 1704.941 908 96(12) | 1602.376 341 36(12) | 12 566.205 259 81(19) |
| 30 | 362.788 279 78(14) | 5030.392 136 75 | 1750.960 624 51(09) | 1648.421 009 91(10) | 12 611.743 318 27(19) |
| 32 | 411.922 496 89(14) | 5078.751 271 32(37) | 1800.095 733 68(12) | 1697.582 538 87(12) | 12 660.364 942 20(20) |
| 34 | 464.171 701 41(15) | 5130.176 204 67(87) | 1852.346 551 55(12) | 1749.859 985 34(12) | 12 712.069 802 86(20) |
| 36 | 519.535 035 94(15) | 5184.666 085 06(167) | 1907.712 340 74(12) | 1805.252 345 88(12) | 12 766.857 624 84(21) |
| 38 | 578.011 591 97(16) | 5242.220 008 16 | 1966.192 328 00(72) | 1863.758 559 96(72) | 12 824.728 187 85(21) |
| 40 | 639.600 409 77(17) | 5302.837 017 11 | 2027.785 696 62(15) | 1925.377 509 00(16) | 12 885.681 334 60(22) |
| 42 | 704.300 478 70(18) | 5366.516 108 31 | 2092.491 583 28(12) | 1990.108 011 91(13) | 12 949.716 977 53(22) |
| 44 | 772.110 736 89(19) | 5433.256 224 68 | 2160.309 085 80(12) | 2057.948 832 81(13) | 13 016.835 102 44(23) |
| 46 | 843.030 071 44(19) | 5503.056 258 05 | 2231.237 261 04(12) | 2128.898 679 03(13) | 13 087.035 783 34(23) |
| 48 | 917.057 318 35(20) | 5575.915 049 97 | 2305.275 121 28(13) | 2202.956 197 43(12) | 13 160.319 193 65(25) |
| 50 | 994.191 262 61(21) | 5651.831 391 27 | 2382.421 636 83(14) | 2280.119 977 14(13) | 13 236.685 625 30(26) |
| 52 | 1074.430 638 19(23) | 5730.804 021 38 | 2462.675 738 23(16) | 2360.388 551 57(14) | 13 316.135 509 92(27) |
| 54 | 1157.774 127 98(26) | 5812.831 628 82 | 2546.036 314 52(21) | 2443.760 396 91(17) | 13 398.669 450 46(29) |
| 56 | 1244.220 364 02(28) | ⋯ | 2632.502 211 82(29) | 2530.233 930 62(23) | 13 484.288 255 56(31) |
| 58 | 1333.767 927 12(30) | ⋯ | 2722.072 236 37(46) | 2619.807 514 07(35) | 13 572.992 994 39(34) |
| 60 | 1426.415 347 38(34) | ⋯ | 2814.745 156 56(83) | 2712.479 456 25(58) | 13 664.785 057 62(39) |
| 62 | 1522.161 103 55(42) | ⋯ | ⋯ | ⋯ | 13 759.666 209 05(42) |
| 64 | 1621.003 624 10(53) | ⋯ | ⋯ | ⋯ | 13 857.638 846 99(49) |
| 66 | 1722.941 285 71(72) | ⋯ | ⋯ | ⋯ | 13 958.705 845 77(59) |
| 68 | 1827.972 414 92(97) | ⋯ | ⋯ | ⋯ | 14 062.871 014 30(84) |
| 70 | 1936.095 288 0(11) | ⋯ | ⋯ | ⋯ | 14 170.139 173 5(11) |
| 72 | 2047.308 128 0(15) | ⋯ | ⋯ | ⋯ | ⋯ |

[a]Denote the ro-vibrational energy level determination type B and C presented in Fig. 4, respectively.

ro-vibrational energy levels determined in TW to those in the new MARVEL and CDSD datasets for both isotopologues.

### 6.1. $^{12}C^{16}O_2$

The MARVEL analysis achieved an accuracy on the order of tens of kilohertz for the 10 011(2), 00 021, 20 012(3), and 30 012(3) states by incorporating saturated absorption experiments. For the 10 001(2) and 00 011 states, however, the uncertainties increase to ~290 kHz. Line positions from the sub-Doppler measurements in the 20 012(3) and 30 012(3) cold bands were compared with predictions from CDSD-2024-PI,[17] UCL-4000,[16] and HITRAN2020.[4] The CDSD-2024-PI predictions approach the experimental accuracy for these transitions, whereas the differences for the other two datasets can exceed the experimental frequency uncertainties by up to three orders of magnitude.

Figure 5 presents the differences between the ro-vibrational energy levels obtained in TW and those from MARVEL[25] [left panels: (a)–(c)] and CDSD-2024-PI[17] [right panels: (d)–(f)]. The differences exhibit distinct characteristics, ranging from tens of kHz to several MHz. For the MARVEL energy levels of the 00 001, 20 012(3), 30 012(3) states in panel (a), the average difference is ~15 kHz. Nevertheless, transition frequencies calculated using the MARVEL energies agree with the experimental frequencies within

**TABLE 4.** High-precision ro-vibrational energy levels of $^{12}C^{16}O_2$: (II) anti-symmetric vibrational states (unit: $cm^{-1}$)

| $J$ | 00 011[a] | 10 011[a] | 10 012[a] | 20 012[a] | 20 013[a] | 30 012[a] | 30 013[a] |
|---|---|---|---|---|---|---|---|
| 1 | 2349.917 070 45(71) | 3715.555 972 6 | 3613.615 709 61(27) | 4978.607 718 792(72) | 4854.399 535 638(80) | 6348.623 796 946(30) | 6228.689 960 617(27) |
| 3 | 2353.788 464 4(10) | 3719.426 588 2 | 3617.490 719 49 | 4982.473 034 298(68) | 4858.281 488 125(73) | 6352.488 333 703(17) | 6232.557 047 554(19) |
| 5 | 2360.756 909 5(10) | 3726.393 637 8(13) | 3624.465 657 65(33) | 4989.430 533 630(69) | 4865.268 911 045(72) | 6359.444 450 554(31) | 6239.517 717 652(21) |
| 7 | 2370.822 287 88(71) | 3736.457 025 7(13) | 3634.540 388 19(27) | 4999.480 099 291(69) | 4875.361 647 252(78) | 6369.492 062 668(32) | 6249.571 822 742(22) |
| 9 | 2383.984 436 02(71) | 3749.616 609 2(13) | 3647.714 714 29 | 5012.621 561 527(80) | 4888.559 470 076(75) | 6382.631 048 149(33) | 6262.719 148 956(26) |
| 11 | 2400.243 133 65(71) | 3765.872 194 3(13) | 3663.988 379 16 | 5028.854 698 805(77) | 4904.862 083 027(84) | 6398.861 248 554(41) | 6278.959 416 965(29) |
| 13 | 2419.598 115 69(71) | 3785.223 558 41(94) | 3683.361 065 33 | 5048.179 237 498(79) | 4924.269 120 315(81) | 6418.182 487 459(34) | 6298.292 281 954(35) |
| 15 | 2442.049 060 75(71) | 3807.670 427 99(94) | 3705.832 395 06(19) | 5070.594 852 351(82) | 4946.780 146 593(79) | 6440.594 424 34(24) | 6320.717 334 103(42) |
| 17 | 2467.595 597 75(71) | 3833.212 481 51(94) | 3731.401 930 36 | 5096.101 166 574(85) | 4972.394 657 52(11) | 6466.096 936 251(48) | 6346.234 098 724(50) |
| 19 | 2496.237 308 7(10) | 3861.849 361 01(94) | 3760.069 173 05(17) | 5124.697 752 353(88) | 5001.112 079 61(12) | 6494.689 639 46(24) | 6374.842 036 619(57) |
| 21 | 2527.973 719 22(71) | 3893.580 659 8(13) | 3791.833 564 75 | 5156.384 130 539(95) | 5032.931 770 68(13) | 6526.372 195 284(83) | 6406.540 544 516(63) |
| 23 | 2562.804 304 6(10) | 3928.405 932 02(95) | 3826.694 487 19 | 5191.159 771 716(96) | 5067.853 020 06(13) | 6561.144 222 546(92) | 6441.328 955 431(69) |
| 25 | 2600.728 493 73(71) | 3966.324 679 0(13) | 3864.651 262 07(25) | 5229.024 096 046(99) | 5105.875 048 91(14) | 6599.005 303 41(25) | 6479.206 539 268(72) |
| 27 | 2641.745 655 89(71) | 4007.336 375 2(13) | 3905.703 151 60(25) | 5269.976 473 81(11) | 5146.997 010 34(14) | 6639.954 983 22(10) | 6520.172 503 201(77) |
| 29 | 2685.855 120 00(71) | 4051.440 438 3 | 3949.849 357 52 | 5314.016 226 06(11) | 5191.217 989 95(15) | 6683.992 772 67(11) | 6564.225 992 389(84) |
| 31 | 2733.056 155 4(10) | 4098.636 246 4(13) | 3997.089 023 07(19) | 5361.142 624 87(11) | 5238.537 006 25(16) | 6731.118 146 67(11) | 6611.366 090 584(87) |
| 33 | 2783.347 984 64(71) | ··· | 4047.421 231 32 | 5411.354 894 06(18) | 5288.953 010 60(16) | 6781.330 544 99(26) | 6661.591 820 803(90) |
| 35 | 2836.729 776 83(71) | ··· | 4100.845 006 30(30) | 5464.652 209 48(11) | 5342.464 888 23(16) | 6834.629 375 03(12) | 6714.902 146 128(94) |
| 37 | 2893.200 652 19(71) | ··· | 4157.359 313 47(27) | 5521.033 700 50(12) | 5399.071 458 16(16) | 6891.014 007 03(27) | 6771.295 970 502(98) |
| 39 | 2952.759 680 1 | ··· | 4216.963 058 36 | 5580.498 449 95(12) | 5458.771 473 92(17) | 6950.483 780 61(13) | 6830.772 139 74(11) |
| 41 | 3015.405 876 9(10) | ··· | 4279.655 088 51 | 5643.045 495 31(13) | 5521.563 623 87(18) | 7013.038 001 54(13) | 6893.329 442 29(11) |
| 43 | 3081.138 207 95(72) | ··· | 4345.434 192 64(21) | 5708.673 830 10(13) | 5587.446 531 65(18) | 7078.675 943 84(28) | 6958.966 610 42(11) |
| 45 | 3149.955 590 66(72) | ··· | 4414.299 101 28 | 5777.382 402 78(14) | 5656.418 756 93(19) | 7147.396 849 46(28) | 7027.682 321 42(12) |
| 47 | 3221.856 890 25(72) | ··· | 4486.248 486 59 | 5849.170 122 83(14) | 5728.478 795 27(20) | 7219.199 930 20(29) | 7099.475 198 69(13) |
| 49 | 3296.840 918 91(72) | ··· | 4561.280 962 76(32) | 5924.035 856 63(15) | 5803.625 079 63(21) | 7294.084 367 28(29) | 7174.343 813 10(14) |
| 51 | 3374.906 439 01(72) | ··· | 4639.395 087 08(37) | 6001.978 432 51(16) | 5881.855 979 87(22) | 7372.049 312 64(30) | 7252.286 684 57(15) |
| 53 | 3456.052 164 38(72) | ··· | 4720.589 357 69 | 6082.996 641 65(25) | 5963.169 803 68(24) | 7453.093 889 10(31) | 7333.302 283 62(16) |
| 55 | 3540.276 755 41(73) | ··· | 4804.862 217 07 | 6167.089 240 65(27) | 6047.564 797 20(25) | 7537.217 192 44(32) | 7417.389 033 07(17) |
| 57 | 3627.578 819 7(10) | ··· | 4892.212 050 10(27) | 6254.254 954 38(29) | 6135.039 145 31(27) | 7624.418 290 22(34) | 7504.545 310 15(19) |
| 59 | 3717.956 921 4(10) | ··· | 4982.637 184 36 | 6344.492 479 51(33) | 6225.590 972 23(30) | 7714.696 224 65(36) | 7594.769 448 57(22) |
| 61 | 3811.409 567 6(10) | ··· | 5076.135 891 94 | 6437.800 489 01(37) | 6319.218 341 69(33) | 7808.050 011 95(39) | 7688.059 741 28(26) |
| 63 | 3907.935 214 7(11) | ··· | 5172.706 388 04 | 6534.177 638 02(44) | 6415.919 258 08(37) | 7904.478 643 64(42) | 7784.414 442 65(30) |
| 65 | 4007.532 271 1(17) | ··· | 5272.346 831 43(64) | 6633.622 571 10(53) | 6515.691 666 04(49) | 8003.981 086 98(50) | 7883.831 772 74(38) |
| 67 | 4110.199 092 0(12) | ··· | 5375.055 327 85(64) | 6736.133 933 13(69) | 6618.533 451 25(56) | 8106.556 286 93(60) | 7986.309 920 36(48) |
| 69 | 4215.933 985 6(12) | ··· | 5480.829 923 29(65) | 6841.710 382 96(94) | 6724.442 441 67(84) | 8212.203 164 74(76) | 8091.847 046 89(66) |
| 71 | 4324.735 203 4(14) | ··· | ··· | 6950.350 613 6(13) | ··· | ··· | 8200.441 295 31(87) |
| 73 | 4436.600 951 2(16) | ··· | ··· | 7062.053 381 6(18) | ··· | ··· | ··· |

[a]Denote the ro-vibrational energy level determination type A and B presented in Fig. 4.

**TABLE 5.** High-precision ro-vibrational energy levels of $^{13}C^{16}O_2$ (unit: $cm^{-1}$)

| $J$ | 00 001 | $J$ | 30 011[a] | 30 012[a] | 30 013[a] | 41 101[a] |
|---|---|---|---|---|---|---|
| 0 | 0.0 | 1 | 6364.395 507 125(33) | 6242.740 838 874(23) | 6120.395 008 640(27) | 6257.792 585 9 |
| 2 | 2.341 418 725 9(03) | 3 | 6368.265 741 7 | 6246.599 343 697(20) | 6124.270 905 624(40) | 6261.686 467 0 |
| 4 | 7.804 691 764 2(33) | 5 | 6375.232 121 414(38) | 6253.544 600 861(20) | 6131.247 428 968(45) | 6268.695 389 0 |
| 6 | 16.389 729 543(10) | 7 | 6385.294 573 8 | 6263.576 521 910(22) | 6141.324 422 515(29) | 6278.819 242 8(15) |
| 8 | 28.096 391 306(17) | 9 | 6398.452 993 831(61) | 6276.694 978 188(26) | 6154.501 660 853(33) | 6292.057 868 3 |
| 10 | 42.924 485 117(23) | 11 | 6414.707 244 180(57) | 6292.899 800 919(31) | 6170.778 849 244(50) | 6308.411 062 90(67) |
| 12 | 60.873 767 860(33) | 13 | 6434.057 155 5 | 6312.190 779 660(39) | 6190.155 624 398(72) | 6327.878 576 0 |
| 14 | 81.943 945 245(40) | 15 | 6456.502 525 582(78) | 6334.567 662 428(45) | 6212.631 553 885(63) | 6350.460 110 82(30) |
| 16 | 106.134 671 807(53) | 17 | 6482.043 119 808(70) | 6360.030 154 112(57) | 6238.206 137 318(72) | 6376.155 329 66(54) |
| 18 | 133.445 550 915(63) | 19 | 6510.678 670 7 | 6388.577 916 327(66) | 6266.878 806 002(77) | 6404.963 850 00(21) |
| 20 | 163.876 134 773(73) | 21 | 6542.408 877 92(10) | 6420.210 566 074(76) | 6298.648 923 985(91) | 6436.885 253 06(31) |
| 22 | 197.425 924 429(83) | 23 | 6577.233 407 57(10) | 6454.927 675 830(86) | 6333.515 787 581(96) | 6471.919 078 56(22) |
| 24 | 234.094 369 778(93) | 25 | 6615.151 891 9 | 6492.728 772 308(96) | 6371.478 626 83(11) | 6510.064 831 2 |
| 26 | 273.880 869 57(10) | 27 | 6656.163 928 28(13) | 6533.613 336 88(11) | 6412.536 605 | 6551.321 979 71(19) |
| 28 | 316.784 771 42(11) | 29 | 6700.269 078 54(14) | 6577.580 804 98(12) | 6456.688 822 | ··· |
| 30 | 362.805 371 81(12) | 31 | 6747.466 866 95(14) | 6624.630 566 69(13) | 6503.934 309 | ··· |
| 32 | 411.941 916 10(13) | 33 | 6797.756 778 50(15) | 6674.761 967 77(13) | 6554.272 036 51(14) | 6693.755 984 56(71) |
| 34 | 464.193 598 54(14) | 35 | 6851.138 255 97(16) | 6727.974 314 17(14) | 6607.700 910 | 6747.452 746 61(36) |
| 36 | 519.559 562 28(15) | 37 | 6907.610 695 95(16) | 6784.266 906 35(15) | 6664.219 772 10(16) | ··· |
| 38 | 578.038 899 38(15) | 39 | 6967.173 442 87(17) | 6843.638 009 21(15) | 6723.827 405 | 6864.170 342 26(57) |
| 40 | 639.630 650 82(16) | 41 | 7029.825 781 35(19) | 6906.089 015 70(16) | 6786.522 528 | ··· |
| 42 | 704.333 806 49(17) | 43 | 7095.566 924 73(20) | 6971.617 211 99(17) | 6852.303 801 58(18) | ··· |
| 44 | 772.147 305 26(18) | 45 | 7164.395 998 84(21) | 7040.222 147 48(18) | 6921.169 828 | 7062.545 882 27(66) |
| 46 | 843.070 034 93(19) | 47 | 7236.312 017 37(22) | 7111.902 888 20(19) | 6993.119 151 | ··· |
| 48 | 917.100 832 28(20) | 49 | ··· | 7186.658 446 67(21) | 7068.150 258 23(22) | ··· |
| 50 | 994.238 483 07(21) | 51 | ··· | 7264.487 797 34(22) | ··· | 7288.861 586 3(17) |
| 52 | 1074.481 722 06(23) | 53 | ··· | 7345.389 881 22(23) | ··· | ··· |
| 54 | 1157.829 233 04(24) | 55 | ··· | 7429.363 609 82(25) | ··· | ··· |
| 56 | 1244.279 648 80(26) | 57 | ··· | 7516.407 869 75(27) | ··· | ··· |
| 58 | 1333.831 551 21(29) | 59 | ··· | 7606.521 527 80(30) | ··· | ··· |
| 60 | 1426.483 471 18(33) | 61 | ··· | 7699.703 439 67(34) | ··· | ··· |
| 62 | 1522.233 888 72(38) | 63 | ··· | ··· | ··· | ··· |

| $J$ | 00 041[a] | $J$ | 00 011[a] |
|---|---|---|---|
| 14 | 9072.964 488 39(19) | 15 | 2376.425 065 36(10) |

[a]Denote the ro-vibrational energy level determination type A presented in Fig. 4, for which the uncertainties are determined by combining the experimental uncertainties of transition frequencies with the calculated uncertainties of the ground-state energy levels.

3.0 kHz for the 20 012(3) and 30 012(3) cold bands. This suggests that the ~15 kHz mean difference originates from the determination of the ground-state energy levels in the MARVEL analysis. A similar explanation applies to the CDSD-2024-PI ro-vibrational energy differences for the 20 012(3) and 30 012(3) states shown in panel (d). For the 00 011 and 10 001(2) states, the average ro-vibrational energy differences are ~470 kHz in the MARVEL analysis [panel (b)] and 90 kHz in the CDSD-2024-PI [panel (e)]. At the same time, both MARVEL and CDSD-2024-PI yield highly accurate frequencies of the 9–10 μm transitions in the 00 011–10 001(2) bands. This indicates that the energy differences in the 10 001(2) states largely arise from discrepancies in the energy levels of the 00 011 state, with the magnitude differing between the two analysis. Different behavior is shown in Figs. 5(c) and 5(f) for the 00 021 and 10 011(2) states. Most of the MARVEL ro-vibrational energies agree the experimental values within 50 kHz for these three vibrational states, whereas the differences in the CDSD-2024-PI range from −4 to 2 MHz and exhibit a strong $J$-dependence.

For the 60 025 state, ro-vibrational energies were not available from either the MARVEL or CDSD-2024-PI results. Instead, they were obtained via kHz-accuracy ladder-type DR absorption spectroscopy (60 025 ← 30 013 ← 00 001, Type b), as reported by Hu *et al.*,[52] rather than through Doppler-limited spectroscopy.

**TABLE 6.** Spectroscopic parameters for 15 vibrational states of $^{12}C^{16}O_2$ and $^{13}C^{16}O_2$ (Unit: MHz)

| | | | $^{12}C^{16}O_2$ | | | |
|---|---|---|---|---|---|---|
| | 00 001 | 10 001[a] | 10 002[a] | 00 011[a] | 10 011[a] | 10 012[a] |
| $G_v$ | ⋯ | 41 616 715.220(10) | 38 535 568.8788(83) | 70 425 529.0568(86) | 111 366 358.075(34) | 108 310 239.5010(46) |
| $B_v$ | 11 698.469 991 0(83) | 11 697.569 597(32) | 11 706.364 719(43) | 11 606.206 960(20) | 11 603.861 78(30) | 11 617.053 162(17) |
| $D_v \times 10^3$ | 3.998 625 2(86) | 3.446 157(24) | 4.712(56) | 3.998 067(10) | 3.425 21(73) | 4.723 714(17) |
| $H_v \times 10^9$ | 0.412 2(33) | 5.716 5(47) | 7.092(25) | 0.443 8(10) | 5.26(48) | 6.691 9(61) |
| $L_v \times 10^{12}$ | −0.000 47(40) | ⋯ | −0.0444(35) | [−0.000 47] | [−0.000 47] | −0.025 36(67) |
| $J_{max}$ | 72 | 60 | 60 | 73 | 31 | 69 |
| $n/N$ | 112 | 29/29 | 29/29 | 58/61 | 18/19 | 23/23 |
| rms | 0.014 | 0.023 | 0.015 | 0.025 | 0.050 | 0.006 8 |
| | 00 021[a] | 20 012[a] | 20 013[a] | 30 012[a] | 30 013[a] | 60 025[a] |
| $G_v$ | 140 102 770.313(23) | 149 231 728.5961(05) | 145 507 961.1574(03) | 190 303 781.7106(73) | 186 708 240.747 32(36) | 367 327 089.5363(42) |
| $B_v$ | 11 514.013 16(16) | 11 587.981 508(06) | 11 637.877 181(04) | 11 585.631 107(25) | 11 593.307 075 1(42) | 11 579.906 32(18) |
| $D_v \times 10^3$ | 3.977 83(31) | 4.080 36(02) | 5.451 34(01) | 2.945 201(31) | 5.143 476(13) | 9.3878(19) |
| $H_v \times 10^9$ | 0.29(17) | 21.87(03) | 18.18(01) | 15.838(17) | 29.728(18) | 3972.0(70) |
| $L_v \times 10^{12}$ | ⋯ | 0.14(02) | −0.032(05) | 0.513 7(40) | 0.209(11) | −1366.2(84) |
| $M_v \times 10^{15}$ | ⋯ | 0.138(09) | −0.025(01) | −0.029 88(34) | 3.02(37) | ⋯ |
| $N_v \times 10^{19}$ | ⋯ | −0.21(02) | −0.009 8(10) | ⋯ | −0.0161(61) | ⋯ |
| $O_v \times 10^{24}$ | ⋯ | 3.1(01) | ⋯ | ⋯ | 0.439(39) | ⋯ |
| $J_{max}$ | 36 | 71 | 69 | 69 | 71 | 20 |
| $n/N$ | 26/26 | 54/63 | 40/43 | 30/56 | 72/72 | 10/10 |
| rms | 0.033 | 0.001 1 | 0.000 8 | 0.006 4 | 0.004 6 | 0.014 |
| | | | $^{13}C^{16}O_2$ | | | |
| | 00 001 | 30 011[a] | 30 012[a] | 30 013[a] | 41 101[a] | |
| $G_v$ | ⋯ | 190 776 571.874 64(66) | 18 712 956.984 24(34) | 183 461 586.934 33(36) | 187 580 554.880(72) | |
| $B_v$ | 11 699.018 560 1(67) | 11 602.706 435(15) | 11 567.549 484 8(83) | 11 619.722 640 0(31) | 11 673.615 68(86) | |
| $D_v \times 10^3$ | 3.996 033 2(44) | 2.520 025(87) | 3.059 634(50) | 5.423 200(07) | 3.827 0(36) | |
| $H_v \times 10^9$ | 0.406 80(81) | −1.20(17) | −124.83(11) | 30.910 0(46) | 177.8(60) | |
| $L_v \times 10^{12}$ | ⋯ | −8.11(11) | 25.781(71) | 0.131 4(10) | −18.3(35) | |
| $J_{max}$ | 61 | 53 | 61 | 49 | 50 | |
| $n/N$ | 26/26 | 14/24 | 21/44 | 21/21 | 12/16 | |
| rms | 0.003 8 | 0.001 8 | 0.002 4 | 0.001 7 | 0.016 | |

[a]Denote the ro-vibrational energy level determination type A, B, and C presented in Fig. 4, respectively. $J_{max}$ denotes the highest measured rotational quantum number.

### 6.2. $^{13}C^{16}O_2$

The frequencies of the 9–10 μm transitions in the 00 011-10 001(2) bands were measured with an accuracy of several kHz by the NIST group in 1986[36] and later updated in 1994.[37] However, the rovibrational energies of the 00 011 (Type A) and 10 001(2) (Type C) states cannot be determined with kHz accuracy because kHz-level experimental frequencies are lacking for the cold band of the 00 011 state. A similar limitation applies to the 00 021 (Type B) and 1001(2) (Type A) states: although kHz-accurate frequencies for the 9–10 μm transitions in the 00 021–1001(2) bands were reported by Chou *et al.*,[38] the corresponding rovibrational energies are still unavailable at that precision. Consequently, only 133 rovibrational energies have been determined with kHz-level accuracy.

Figure 6 shows the differences between the TW rovibrational energy levels and those from MARVEL[26] for the 00 001 state [panel (a)], the 3001(2,3) states [panel (b)], and the 41 101 state [panel (c)]. The ground-state energy differences range from −10 kHz to 1.6 MHz and exhibit a pronounced J-dependence. For the other four vibrational states, the differences vary between −100 and 100 MHz.

For $^{13}C^{16}O_2$, the accuracy of the MARVEL analysis for the 30 011(2,3) and 41 101 vibrational states remains at the level of several to tens of MHz, owing to the absence of kHz-accurate experimental line positions in their dataset.[26] While most of the present energies fall within the 3-$\sigma$ MARVEL uncertainty bounds, eight energies in the 30 012 state lie outside the 3-$\sigma$ range. This discrepancy highlights that the reliability of MARVEL uncertainty estimates depends strongly on the availability of high-accuracy experimental data and may occasionally be underestimated when the analysis incorporates only Doppler-limited measurements.

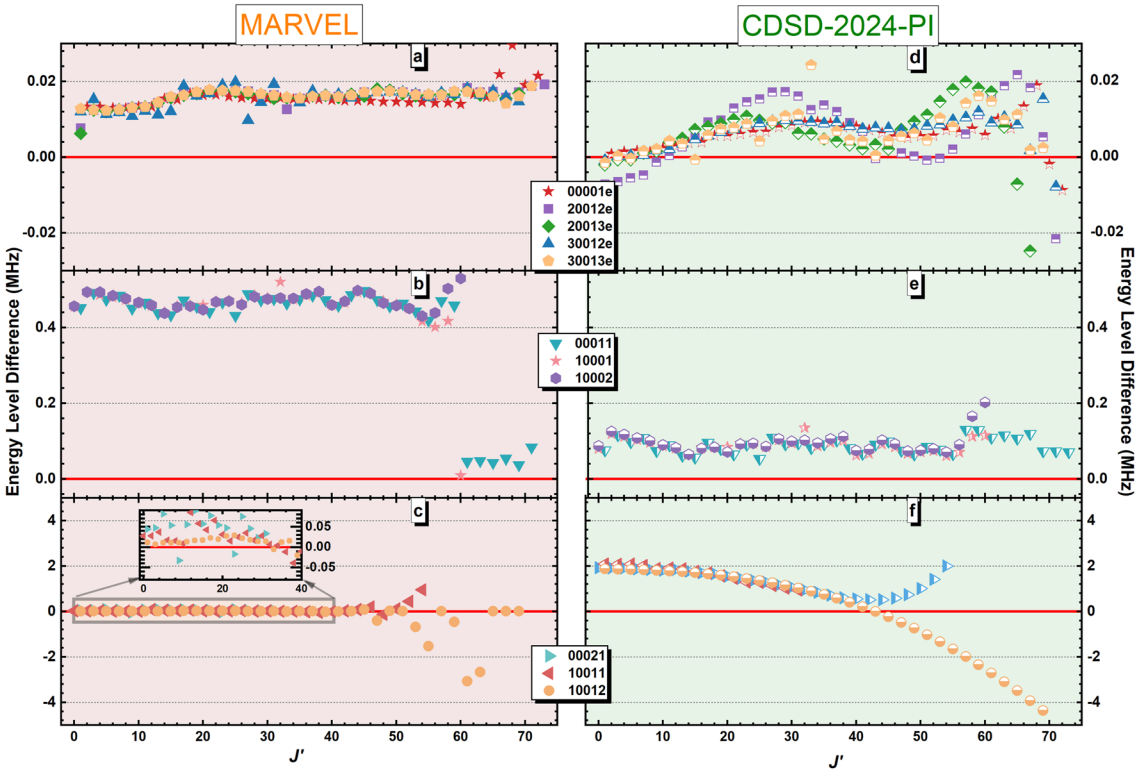


**FIG. 5.** Energy level differences between the values obtained in TW and those from MARVEL[25] (left panels) and from CDSD-2024-PI version[17] (right panels) are plotted against the rotational quantum number $J'$ for 11 vibrational states of $^{12}C^{16}O_2$. These are presented as follows: panels (a) and (d), states 00 001, 20 012(3) and 30 012(3); panels (b) and (e), states 00 011 and 10 001(2); panels (c) and (f), states 00 021 and 10 011(2).

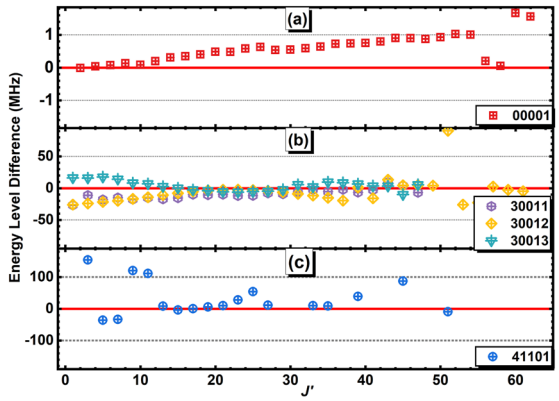


**FIG. 6.** Energy level differences between the results of TW and the MARVEL values[26] are plotted against the rotational quantum number $J'$ for five vibrational states of $^{13}C^{16}O_2$, presented in three panels: (a) 00 001, (b) 30 011/30 012/30 013, and (c) 41 101.

## 7. Conclusion

In summary, we have developed and demonstrated an optical-frequency-comb-stabilized cavity-enhanced V-type DR (COCA-DR) spectroscopy technique for the kilohertz-accuracy measurement of extremely weak rovibrational transitions in $CO_2$ isotopologues. By pumping a strong transition while probing a weak counterpart, this method significantly reduces the required intra-cavity laser power by 2–3 orders of magnitude and enhances the signal-to-noise ratio by approximately one order of magnitude compared to conventional saturation spectroscopy. We measured 18 transitions in the 41 101–00 001 band of $^{13}C^{16}O_2$ with uncertainties ranging from 4 to 52 kHz. Combined with three distinct computational models for ro-vibrational energy levels, we derived a total of 394 and 133 experimental rovibrational energy levels for $^{12}C^{16}O_2$ (12 vibrational states) and $^{13}C^{16}O_2$ (7 vibrational states), respectively, with energies up to 14 170 $cm^{-1}$.

All energy levels are based on sub-Doppler measurements and exhibit significantly higher accuracy than those derived from existing spectroscopic databases such as MARVEL and CDSD, which rely partly on Doppler-limited data. The presented energy-level sets provide crucial benchmarks for refining high-accuracy spectroscopic databases (e.g., HITRAN, CDSD, MARVEL) and will enhance the precision of atmospheric remote-sensing retrievals for climate monitoring, planetary science, and exoplanet characterization. This DR approach, applicable also to other polyatomic molecules, opens a pathway for systematic precision measurements of weak and forbidden transitions, supporting the continued advancement of molecular spectroscopy and its applications.

## Acknowledgments

This work was jointly supported by the National Natural Science Foundation of China (Grant Nos. 22273096 and 22327801), Quantum Science and Technology-National Science and Technology Major Project (Grant Nos. 2021ZD0303102, 2021ZD0303304, and 2023ZD0301002).

## 8. Author Declarations

### 8.1. Conflict of interest

The authors have no conflicts to disclose.

## 9. Data Availability

The data that support the findings of this study are available from the corresponding author upon reasonable request.

## 10. Appendix: Depth of Sub-Doppler Signal

### 10.1. Depth of weak saturated signal

The saturated depth $d_S$ of the weak transition 2 is approximated as

$$d_S \approx \alpha_2^0\left(\frac{1}{\sqrt{1+S}}-\frac{1}{\sqrt{1+2S}}\right)\approx \alpha_2^0\frac{S}{2}. \tag{A1}$$

Here, the unsaturated absorption coefficient $\alpha_2^0$ and the saturation coefficient $S$ can be expressed, following the definitions of line intensity[4] and saturation intensity[39] $I_s$,

$$\alpha_2^0 = N\frac{A_2}{8\pi^{3/2}\omega_2^3}\frac{g_2' e^{-E_2''/k_BT}(1-e^{-h\omega_2/k_BT})}{Q(T)}\sqrt{\frac{m}{2k_BT}}$$
$$S = I/I_S = I\frac{3A_2}{8\pi^3 ch\omega_2^3\Gamma^2} \tag{A2}$$

where $N$ is the molecular density, $A_2$ (in $s^{-1}$) is the Einstein-A coefficient of weak transition at frequency $\omega_2$ (in $cm^{-1}$), $E_2''$ (in $cm^{-1}$) is the lower-state energy of weak transition, $g_2'$ is the statistical weight of the upper state, $Q(T)$ is the total internal partition sum, $I$ is the laser intensity, $\Gamma$ (in $cm^{-1}$) is the FWHM of the transition, $c$ is the speed of light, $h$ is Planck's constant, and $k_B$ is Boltzmann's constant.

By defining a parameter $\beta$ that consolidates fundamental constants, certain molecular properties unrelated to the considered transitions, and some experimental parameters,

$$\beta \approx N\frac{3}{64\pi^{9/2}}\frac{e^{-E_2''/k_BT}}{chQ(T)}\sqrt{\frac{m}{2k_BT}}. \tag{A3}$$

The depth $d_S$ can be rewritten as

$$d_S \approx \beta\frac{IA_2^2 g_2'}{2\Gamma^2}\frac{1}{\omega_2^6}. \tag{A4}$$

### 10.2. Depth of DR signal

In a V-type DR process, when the pump laser at frequency $\omega_1$ is applied, molecules in the lower state 0 with axial velocity $V_z$ are transferred to the upper state 1. According to the reduction in population density $N_0(V_z)dV_z$ reduction within the velocity interval $dv_z$ as given by Eq. 2.24(a),[66] the population difference in the probe transition at $\omega_2$ can be expressed as

$$\Delta N_{02}(v_z) = \underbrace{N_0^0(v_z)-\frac{g_0}{g_2}N_2^0(v_z)}_{\Delta N_2^0(v_z)} - \underbrace{\frac{\Delta N_1^0(v_z)}{2}\left[\frac{S_1(\Gamma/2)^2}{(\omega_1-\omega_{10}-k_1(\pm v_z))^2+(1+S_1)(\Gamma/2)^2}\right]}_{\Delta N_2^{DR}(\omega_2,\pm v_z)}. \tag{A5}$$

The first term on the right, $\Delta N_2^0(v_z)$, denotes the population difference for the probe transition $0 \to 2$ under thermal equilibrium, representing the conventional Doppler-broadened absorption. The second term, $\Delta N_2^{DR}(\omega_2, \pm v_z)$, describes the population difference associated with the DR signal. Here, $g_0$ and $g_2$ are the statistical weights of states 0 and 2, respectively; $k_1$ is the wave vector of the pump laser, and $S_1$ is the saturation coefficient for transition 1. The $\pm$ sign corresponds to the situations where the pump and probe lasers are co-propagating or counter-propagating.

Considering molecules with velocities between $V_z$ and $V_z + dV_z$, the absorption coefficient for the probe transition at $\omega_2$ is given by

$$\alpha(\omega_2) = \underbrace{\int \Delta N_2^0(V_z)\sigma_2(\omega_2,V_z)dV_z}_{\alpha_2^0(\omega_2)} - \underbrace{\int \Delta N_2^{DR}(\omega_1,\pm V_z)\sigma_2^0\frac{(\Gamma/2)^2}{(\omega_2-\omega_{20}-k_2V_z)^2+(\Gamma/2)^2}dV_z}_{\alpha_2^{DR}(\omega_1,\omega_2)}. \tag{A6}$$

Here, $\alpha_2^0(\omega_2)$ and $\alpha_2^{DR}(\omega_1,\omega_2)$ correspond to the conventional absorption and the DR signal, respectively. For a Boltzmann distribution velocity and weak field regime, the integrated DR signal $\alpha_2^{DR}(\omega_1,\omega_2)$ can be approximated as

$$\alpha_2^0(\omega_2)\frac{\omega_2 S_1}{\omega_1\sqrt{1+S}}\frac{\Gamma^2}{\left(\omega_2-\omega_{20}\mp\frac{\omega_2}{\omega_1}(\omega_1-\omega_{10})\right)^2+\Gamma^2}. \tag{A7}$$

Substituting Eq. (A2) into Eq. (A7) yields the DR depth for V-type DR spectroscopy as

$$d_D \approx \alpha_2^0(\omega_2)\frac{\omega_2 S_1}{\omega_1\sqrt{1+S}} \approx \alpha_2^0(\omega_2)\frac{\omega_2}{\omega_1}S_1 \qquad (S\ll 1)$$
$$= \beta\frac{I_{\text{pump}}A_1A_2g_2'}{\Gamma^2}\frac{1}{\omega_1^4\omega_2^2}. \tag{A8}$$

If, instead, the weak transition at $\omega_2$ is pumped and another transition at $\omega_1$ is probed, the DR depth in V-typ DR spectroscopy $d_D$ becomes $d_D \approx \beta\frac{I_{\text{pump}}A_1A_2g_1'}{\Gamma^2}\frac{1}{\omega_1^2\omega_2^4}$.

Following a similar derivation, the DR depth for the Λ-type system, in which Transition 2 serves as the probe, is

$$d_S \approx \beta \frac{I_{\text{pump}} A_1 A_2 g_2'}{\Gamma^2} \frac{1}{\omega_1^4 \omega_2^2} \exp\left(-\frac{\Delta E}{k_B T}\right). \quad \text{(A9)}$$

## 11. References


[1] D. C. Catling and J. F. Kasting, *Atmospheric Evolution on Inhabited and Lifeless Worlds* (Cambridge University Press, Cambridge, 2017).

[2] S. Arrhenius, "On the influence of carbonic acid in the air upon the temperature of the Earth," Publ. Astron. Soc. Pac. **9**, 14–24 (1897).

[3] P. A. Arias, N. Bellouin, E. Coppola, R. G. Jones, G. Krinner, J. Marotzke, V. Naik, M. D. Palmer, G.-K. Plattner, J. Rogelj *et al.*, "Technical summary," in *Climate Change 2021: The Physical Science Basis: Contribution of Working Group I to the Sixth Assessment Report of the Intergovernmental Panel on Climate Change*, edited by V. Masson-Delmotte, P. Zhai, A. Pirani, S. Connors, C. Péan, S. Berger, N. Caud, Y. Chen, L. Goldfarb, M. Gomis, M. Huang, K. Leitzell, E. Lonnoy, J. Matthews, T. Maycock, T. Waterfield, O. Yelekçi, R. Yu, and B. Zhou (Cambridge University Press, Cambridge, 2021), pp. 33–144.

[4] I. E. Gordon, L. S. Rothman, R. J. Hargreaves, R. Hashemi, E. V. Karlovets, F. M. Skinner, E. K. Conway, C. Hill, R. V. Kochanov, Y. Tan *et al.*, "The HITRAN2020 molecular spectroscopic database," J. Quant. Spectrosc. Radiat. Transfer **277**, 107949 (2022).

[5] T. Delahaye, R. Armante, N. A. Scott, N. Jacquinet-Husson, A. Chédin, L. Crépeau, C. Crevoisier, V. Douet, A. Perrin, A. Barbe *et al.*, "The 2020 edition of the GEISA spectroscopic database," J. Mol. Spectrosc. **380**, 111510 (2021).

[6] World Meteorological Organization, WMO Greenhouse Gas Bulletin (No. 21): The State of Greenhouse Gases in the Atmosphere Based on Global Observations through 2024, Geneva, Switzerland, 2025.

[7] R. D. Wordsworth and R. T. Pierrehumbert, "Water loss from terrestrial planets with $CO_2$-rich atmospheres," Astrophys. J. **778**, 154 (2013).

[8] A. Eldering, T. E. Taylor, C. W. O'Dell, and R. Pavlick, "The OCO-3 mission: Measurement objectives and expected performance based on 1 year of simulated data," Atmos. Meas. Tech. **12**, 2341–2370 (2019).

[9] H. Tanimoto, T. Matsunaga, Y. Someya, T. Fujinawa, H. Ohyama, I. Morino, H. Yashiro, T. Sugita, S. Inomata, A. Müller *et al.*, "The greenhouse gas observation mission with Global Observing SATellite for Greenhouse gases and Water cycle (GOSAT-GW): Objectives, conceptual framework and scientific contributions," Prog. Earth Planet. Sci. **12**, 8 (2025).

[10] J. M. Hobbs, B. J. Drouin, F. Oyafuso, V. H. Payne, M. R. Gunson, J. McDuffie, and E. J. Mlawer, "Spectroscopic uncertainty impacts on OCO-2/3 retrievals of $XCO_2$," J. Quant. Spectrosc. Radiat. Transfer **257**, 107360 (2020).

[11] S. Noël, M. Buchwitz, M. Hilker, M. Reuter, M. Weimer, H. Bovensmann, J. P. Burrows, H. Bösch, and R. Lang, "Greenhouse gas retrievals for the CO2M mission using the FOCAL method: First performance estimates," Atmos. Meas. Technol. **17**, 2317–2334 (2024).

[12] R. Hu, D. M. Kass, B. L. Ehlmann, and Y. L. Yung, "Tracing the fate of carbon and the atmospheric evolution of Mars," Nat. Commun. **6**, 10003 (2015).

[13] M. Snels, S. Stefani, D. Grassi, G. Piccioni, and A. Adriani, "Carbon dioxide opacity of the Venus' atmosphere," Planet. Space Sci. **103**, 347–354 (2014).

[14] S. A. Tashkun, V. I. Perevalov, R. R. Gamache, and J. Lamouroux, "CDSD-296, high-resolution carbon dioxide spectroscopic databank: An update," J. Quant. Spectrosc. Radiat. Transfer **228**, 124–131 (2019).

[15] X. Huang, D. W. Schwenke, R. S. Freedman, and T. J. Lee, "Ames-2021 $CO_2$ dipole moment surface and ir line lists: Toward 0.1% uncertainty for $CO_2$ IR intensities," J. Phys. Chem. A **126**, 5940–5964 (2022).

[16] S. N. Yurchenko, T. M. Mellor, R. S. Freedman, and J. Tennyson, "ExoMol line lists – XXXIX. Ro-vibrational molecular line list for $CO_2$," Mon. Not. R. Astron. Soc. **496**, 5282–5291 (2020).

[17] R. V. Kochanov and V. I. Perevalov, "CDSD-2024-PI: The update of the CDSD databank for the principal isotopologue of carbon dioxide," J. Quant. Spectrosc. Radiat. Transfer **341**, 109428 (2025).

[18] A. G. Császár and T. Furtenbacher, "Spectroscopic networks," J. Mol. Spectrosc. **266**, 99–103 (2011).

[19] T. Furtenbacher, A. G. Császár, and J. Tennyson, "MARVEL: Measured active rotational–vibrational energy levels," J. Mol. Spectrosc. **245**, 115–125 (2007).

[20] T. Furtenbacher, P. Árendás, G. Mellau, and A. G. Császár, "Simple molecules as complex systems," Sci. Rep. **4**, 4654 (2014).

[21] T. Furtenbacher, R. Tóbiás, J. Tennyson, O. L. Polyansky, and A. G. Császár, "W2020: A database of validated rovibrational experimental transitions and empirical energy levels of $H_2^{16}O$," J. Phys. Chem. Ref. Data **49**, 033101 (2020).

[22] T. Furtenbacher, R. Tóbiás, J. Tennyson, R. R. Gamache, and A. G. Császár, "The W2024 database of the water isotopologue $H_2^{16}O$," Sci. Data **11**, 1058 (2024).

[23] R. Tóbiás, M. L. Diouf, F. M. J. Cozijn, W. Ubachs, and A. G. Császár, "All paths lead to hubs in the spectroscopic networks of water isotopologues $H_2^{16}O$ and $H_2^{18}O$," Commun. Chem. **7**, 34 (2024).

[24] M. L. Diouf, R. Tóbiás, I. Simkó, F. M. J. Cozijn, E. J. Salumbides, W. Ubachs, and A. G. Császár, "Network-based design of near-infrared lamb-dip experiments and the determination of pure rotational energies of $H_2^{18}O$ at kHz accuracy," J. Phys. Chem. Ref. Data **50**, 023106 (2021).

[25] A. A. A. Azzam, D. Alatoom, B. M. J. Abou Doud, M. Q. A. Shersheer, B. K. M. Almasri, C. N. M. Bader, B. O. A. K. Musleh, M. Z. J. Obaido, A. M. H. Abu Khudair, A. W. M. Al Shatarat, B. I. M. Qattan, L. H. M. Hamamsy, A. O. G. Saafneh, M. N. A. ALso'ub, M. M. A. Alkhashashneh, H. O. M. Al-Zawahra, M. T. I. Ibrahim, J. Tennyson, S. N. Yurchenko, T. Furtenbacher, and A. G. Császár, "The 626M24 dataset of validated transitions and empirical rovibrational energy levels of $^{16}O^{12}C^{16}O$," Sci. Data **12**, 532 (2025).

[26] M. T. I. Ibrahim, D. Alatoom, T. Furtenbacher, A. G. Császár, S. N. Yurchenko, A. A. A. Azzam, and J. Tennyson, "MARVEL analysis of high-resolution rovibrational spectra of $^{13}C^{16}O_2$," J. Comput. Chem. **45**, 969–984 (2024).

[27] D. Alatoom, M. T. I. Ibrahim, T. Furtenbacher, A. G. Császár, M. Alghizzawi, S. N. Yurchenko, A. A. A. Azzam, and J. Tennyson, "MARVEL analysis of high-resolution rovibrational spectra of $^{16}O^{12}C^{18}O$," J. Comput. Chem. **45**, 2558–2573 (2024).

[28] A. A. A. Azzam, J. Tennyson, S. N. Yurchenko, T. Furtenbacher, and A. G. Császár, "MARVEL analysis of high-resolution rovibrational spectra of $^{16}O^{13}C^{18}O$," J. Comput. Chem. **46**, e27541 (2025).

[29] A. A. A. Azzam, S. A. A. Azzam, K. A. A. Aburumman, J. Tennyson, S. N. Yurchenko, A. G. Császár, and T. Furtenbacher, "MARVEL analysis of high-resolution rovibrational spectra of the $^{18}O^{12}C^{18}O$, $^{17}O^{12}C^{18}O$, and $^{18}O^{13}C^{18}O$ isotopologues of carbon dioxide," J. Mol. Spectrosc. **405**, 111947 (2024).

[30] M. H. I. Mansour, A. B. I. Al-Iter, A. A. A. Azzam, J. Tennyson, T. Furtenbacher, and A. G. Császár, "MARVEL analysis of high-resolution rovibrational spectra of $^{16}O^{13}C^{17}O$ and $^{17}O^{12}C^{17}O$," Mol. Phys. (published online 2025).

[31] K. Kefala, V. Boudon, S. N. Yurchenko, and J. Tennyson, "Empirical rovibrational energy levels for methane," J. Quant. Spectrosc. Radiat. Transfer **316**, 108897 (2024).

[32] T. Turányi, I. G. Zsély, M. Papp, T. Nagy, T. Furtenbacher, R. Tóbiás, P. Árendás, and A. G. Császár, "ReSpecTh: Reaction kinetics, spectroscopy, and thermochemical datasets," Sci. Data **12**, 1021 (2025).

[33] A. Gambetta, E. Fasci, A. Castrillo, M. Marangoni, G. Galzerano, G. Casa, P. Laporta, and L. Gianfrani, "Frequency metrology in the near-infrared spectrum of $H_2^{17}O$ and $H_2^{18}O$ molecules: testing a new inversion method for retrieval of energy levels," New J. Phys. **12**, 103006 (2010).

[34] E. Fasci, S. Gravina, G. Porzio, A. Castrillo, and L. Gianfrani, "Lamb-dip cavity ring-down spectroscopy of acetylene at 1.4 $\mu$m," New J. Phys. **23**, 123023 (2021).

[35] A. Castrillo, E. Fasci, T. Furtenbacher, V. D'Agostino, M. A. Khan, S. Gravina, L. Gianfrani, and A. G. Császár, "On the $^{12}C_2H_2$ near-infrared spectrum: Absolute transition frequencies and an improved spectroscopic network at the kHz accuracy level," Phys. Chem. Chem. Phys. **25**, 23614–23625 (2023).

[36] L. Bradley, K. Soohoo, and C. Freed, "Absolute frequencies of lasing transitions in nine $CO_2$ isotopic species," IEEE J. Quantum Electron. **22**, 234–267 (1986).

[37] A. G. Maki, C. C. Chou, K. M. Evenson, L. R. Zink, and J. T. Shy, "Improved molecular constants and frequencies for the $CO_2$ laser from new high-$J$ regular and hot-band frequency measurements," J. Mol. Spectrosc. **167**, 211–224 (1994).

[38]C. C. Chou, A. G. Maki, S. J. Tochitsky, J. T. Shy, K. M. Evenson, and L. R. Zink, "Frequency measurements and molecular constants of $CO_2$ $00^0 2$-$[10^0 1, 02^0 1]_{I,II}$ sequence band transitions," J. Mol. Spectrosc. **172**, 233–242 (1995).
[39]G. Giusfredi, S. Bartalini, S. Borri, P. Cancio, I. Galli, D. Mazzotti, and P. De Natale, "Saturated-absorption cavity ring-down spectroscopy," Phys. Rev. Lett. **104**, 110801 (2010).
[40]J. Burkart, T. Sala, D. Romanini, M. Marangoni, A. Campargue, and S. Kassi, "Saturated $CO_2$ absorption near 1.6 $\mu$m for kilohertz-accuracy transition frequencies," J. Chem. Phys. **142**, 191103 (2015).
[41]J. Wang, Y. R. Sun, L. G. Tao, A. W. Liu, and S. M. Hu, "Communication: Molecular near-infrared transitions determined with sub-kHz accuracy," J. Chem. Phys. **147**, 091103 (2017).
[42]H. Wu, C.-L. Hu, J. Wang, Y. R. Sun, Y. Tan, A.-W. Liu, and S.-M. Hu, "A well-isolated vibrational state of $CO_2$ verified by near-infrared saturated spectroscopy with kHz accuracy," Phys. Chem. Chem. Phys. **22**, 2841–2848 (2020).
[43]Y. Tan, Y. R. Xu, T. P. Hua, A. W. Liu, J. Wang, Y. R. Sun, and S. M. Hu, "Cavity-enhanced saturated absorption spectroscopy of the (30012)-(00001) band of $^{12}C^{16}O_2$," J. Chem. Phys. **156**, 044201 (2022).
[44]H. Fleurbaey, P. Čermák, A. Campargue, S. Kassi, D. Romanini, O. Votava, and D. Mondelain, "$^{12}CO_2$ transition frequencies with kHz-accuracy by saturation spectroscopy in the 1.99–2.09 μm region," Phys. Chem. Chem. Phys. **25**, 16319–16330 (2023).
[45]S. Jiang, Y. Tan, A. W. Liu, X. G. Zhou, and S. M. Hu, "Saturated cavity ring-down spectroscopy of $^{12}C^{16}O_2$ near 1.57 $\mu$m," Chin. J. Chem. Phys. **37**, 13–18 (2024).
[46]Z. T. Zhang, F. H. Cao, S. Jiang, A. W. Liu, Y. Tan, Y. R. Sun, and S. M. Hu, "Rovibrational energies of $^{13}C^{16}O_2$ determined with kilohertz accuracy," J. Phys. Chem. A **128**, 2366–2375 (2024).
[47]Y. N. Lv, A. W. Liu, Y. Tan, C. L. Hu, T. P. Hua, X. B. Zou, Y. R. Sun, C. L. Zou, G. C. Guo, and S. M. Hu, "Fano-like resonance due to interference with distant transitions," Phys. Rev. Lett. **129**, 163201 (2022).
[48]A. Foltynowicz, L. Rutkowski, I. Silander, A. C. Johansson, V. Silva de Oliveira, O. Axner, G. Soboń, T. Martynkien, P. Mergo, and K. K. Lehmann, "Sub-Doppler double-resonance spectroscopy of methane using a frequency comb probe," Phys. Rev. Lett. **126**, 063001 (2021).
[49]S. Okubo, H. Inaba, S. Okuda, and H. Sasada, "Frequency measurements of the $2\nu_3 A_1 - \nu_3$ band transitions of methane in comb-referenced infrared-infrared double-resonance spectroscopy," Phys. Rev. A **103**, 022809 (2021).
[50]V. S. de Oliveira, I. Silander, L. Rutkowski, G. Sobon, O. Axner, K. K. Lehmann, and A. Foltynowicz, "Sub-Doppler optical-optical double-resonance spectroscopy using a cavity-enhanced frequency comb probe," Nat. Commun. **15**, 161 (2024).
[51]C.-L. Hu, J. Wang, T.-P. Hua, A.-W. Liu, Y. R. Sun, and S.-M. Hu, "Comb-locked cavity-assisted double-resonance molecular spectroscopy based on diode lasers," Rev. Sci. Instrum. **92**, 073003 (2021).
[52]C.-L. Hu, V. I. Perevalov, C.-F. Cheng, T.-P. Hua, A.-W. Liu, Y. R. Sun, Y. Tan, J. Wang, and S.-M. Hu, "Optical-optical double-resonance absorption spectroscopy of molecules with kilohertz accuracy," J. Phys. Chem. Lett. **11**, 7843–7848 (2020).
[53]L. S. Ma, J. Ye, P. Dubé, and J. L. Hall, "Ultrasensitive frequency-modulation spectroscopy enhanced by a high-finesse optical cavity: Theory and application to overtone transitions of $C_2H_2$ and $C_2HD$," J. Opt. Soc. Am. B **16**, 2255–2268 (1999).
[54]C.-F. Cheng and S.-M. Hu, "Cavity-enhanced excitation of molecules with continuous-wave lasers," Chin. J. Chem. Phys. **39**, 9–21 (2026).
[55]V. S. De Oliveira, A. Hjältén, I. Silander, A. Rosina, M. Rey, K. K. Lehmann, and A. Foltynowicz, "Combined frequency comb and continuous wave cavity-enhanced optical-optical double-resonance spectrometer in the 1.7 μm range," Opt. Express **33**, 38776 (2025).
[56]F. M. J. Cozijn, P. Dupré, E. J. Salumbides, K. S. E. Eikema, and W. Ubachs, "Sub-Doppler frequency metrology in HD for tests of fundamental physics," Phys. Rev. Lett. **120**, 153002 (2018).
[57]L. G. Tao, A. W. Liu, K. Pachucki, J. Komasa, Y.. Sun, J. Wang, and S.-M. Hu, "Toward a determination of the proton-electron mass ratio from the lamb-dip measurement of HD," Phys. Rev. Lett. **120**, 153001 (2018).
[58]F. M. J. Cozijn, M. L. Diouf, and W. Ubachs, "Saturation spectroscopy of R(0), R(2) andP(2) lines in the (2-0) band of HD," Eur. Phys. J. D **76**, 220 (2022).
[59]F. M. J. Cozijn, M. L. Diouf, and W. Ubachs, "Lamb dip of a quadrupole transition in $H_2$," Phys. Rev. Lett. **131**, 073001 (2023).
[60]B. V. Perevalov, V. I. Perevalov, and A. Campargue, "A (nearly) complete experimental linelist for $^{13}C^{16}O_2$, $^{16}O^{13}C^{18}O$,$^{16}O^{13}C^{17}O$,$^{13}C^{18}O_2$ and $^{17}O^{13}C^{18}O$ by high-sensitivity CW-CRDS spectroscopy between 5851 and 7045 $cm^{-1}$," J. Quant. Spectrosc. Radiat. Transfer **109**, 2437–2462 (2008).
[61]I. E. Gordon, L. S. Rothman, R. J. Hargreaves, F. M. Gomez, T. Bertin, C. Hill, R. V. Kochanov, Y. Tan, P. Wcisło, V. Y. Makhnev, P. F. Bernath, M. Birk, V. Boudon, A. Campargue, A. Coustenis, B. J. Drouin, R. R. Gamache, J. T. Hodges, D. Jacquemart, E. J. Mlawer, A. V. Nikitin, V. I. Perevalov, M. Rotger, S. Robert, J. Tennyson, G. C. Toon, H. Tran, V. G. Tyuterev, E. M. Adkins, A. Barbe, D. M. Bailey, K. Bielska, L. Bizzocchi, T. A. Blake, C. A. Bowesman, P. Cacciani, P. Čermák, A. G. Császár, L. Denis, S. C. Egbert, O. Egorov, A. Y. Ermilov, A. J. Fleisher, H. Fleurbaey, A. Foltynowicz, T. Furtenbacher, M. Germann, E. R. Guest, J. J. Harrison, J.-M. Hartmann, A. Hjältén, S.-M. Hu, X. Huang, T. J. Johnson, H. Jóźwiak, S. Kassi, M. V. Khan, F. Kwabia-Tchana, T. J. Lee, D. Lisak, A.-W. Liu, O. M. Lyulin, N. A. Malarich, L. Manceron, A. A. Marinina, S. T. Massie, J. Mascio, E. S. Medvedev, V. V. Meshkov, G. C. Mellau, M. Melosso, S. N. Mikhailenko, D. Mondelain, H. S. P. Müller, M. O'Donnell, A. Owens, A. Perrin, O. L. Polyansky, P. L. Raston, Z. D. Reed, M. Rey, C. Richard, G. B. Rieker, C. Röske, S. W. Sharpe, E. Starikova, N. Stolarczyk, A. V. Stolyarov, K. Sung, F. Tamassia, J. Terragni, V. G. Ushakov, S. Vasilchenko, B. Vispoel, K. L. Vodopyanov, G. Wagner, S. Wójtewicz, S. N. Yurchenko, and N. F. Zobov, "The HITRAN2024 molecular spectroscopic database," J. Quant. Spectrosc. Radiat. Transfer **353**, 109807 (2026).
[62]C.-C. Liao, K. Y. Wu, Y. H. Lien, and J. T. Shy, "High precision mid-ir spectroscopy of $^{12}C^{16}O_2$: $00^01 \leftarrow 00^00$ band near 4.3 $\mu$m," in Proceedings of the 63rd Ohio State University International Symposium on Molecular Spectroscopy, Columbus, OH, 2008.
[63]K.-Y. Wu, C.-C. Liao, Y.-H. Lien, and J.-T. Shy, "High precision mid-IR spectroscopy of $^{12}C^{16}O_2$: $[10^01, 02^01]_I \leftarrow 00^00$ band near 2.7 $\mu$m," in Proceedings of the 63rd Ohio State University International Symposium on Molecular Spectroscopy, Columbus, Ohio, 2008.
[64]Y.-C. Guan, D. N. Patel, B.-H. Peng, T.-H. Suen, L.-B. Wang, and J.-T. Shy, "Frequency measurements and molecular constants of the $^{12}C^{16}O_2$ $[10^01, 02^01]_{II} \leftarrow 00^00$ band near 2.7 $\mu$m," J. Mol. Spectrosc. **334**, 26–30 (2017).
[65]Y.-D. Tan, C.-F. Cheng, Y. Tan, and S.-M. Hu, "Mid-infrared-near-infrared double-resonance spectroscopy of molecules with kilohertz accuracy," Opt. Lett. **49**, 1109 (2024).
[66]W. Demtröder, *Laser Spectroscopy: Volume 2 Technology* (Springer, 2008).